Clemson University
TigerPrints

All Theses | Theses

5-2017

Investigation of the Contribution of Lower Charger State Ar Ions to the Unknown Faint X-Ray Feature Found in the Stacked Spectrum of Galaxy Clusters

Amy Gall
Clemson University, acgall@clemson.edu

Follow this and additional works at: https://tigerprints.clemson.edu/all_theses

Recommended Citation
Gall, Amy, "Investigation of the Contribution of Lower Charger State Ar Ions to the Unknown Faint X-Ray Feature Found in the Stacked Spectrum of Galaxy Clusters" (2017). *All Theses*. 2626.
https://tigerprints.clemson.edu/all_theses/2626

This Thesis is brought to you for free and open access by the Theses at TigerPrints. It has been accepted for inclusion in All Theses by an authorized administrator of TigerPrints. For more information, please contact kokeefe@clemson.edu.

INVESTIGATION OF THE CONTRIBUTION OF LOWER CHARGER STATE AR IONS TO THE UNKNOWN FAINT X-RAY FEATURE FOUND IN THE STACKED SPECTRUM OF GALAXY CLUSTERS

A Thesis
Presented to
the Graduate School of
Clemson University

In Partial Fulfillment
of the Requirements for the Degree
Master of Science
Physics

---

by
Amy Gall
May 2017

Accepted by:
Dr. Endre Takacs, Committee Chair
Dr. Marco Ajello
Dr. Chad Sosolik

ABSTRACT

Driven by the recent detection of an unidentified emission line previously reported at 3.55-3.57 keV in a stacked spectrum of galaxy clusters, in this work we investigated the resonant dielectronic recombination (DR) process in Li-like Ar as a possible source of, or contributor to, the emission line. The Li-like transition $1s^2 2l\text{-}1s2l3l'$ was suggested to produce a 3.62 keV photon [1] near the unidentified line at 3.57 keV and was the primary focus of our study. The Electron Beam Ion Trap at NIST was used to produce and trap the highly-charged ions of argon. The energy of the quasi-monoenergetic electron beam was incremented in steps of 15 eV to scan over all of the Li-like Ar DR resonances. A Johann-type crystal spectrometer and a solid-state germanium detector were used to take x-ray measurements perpendicular to the electron beam. Our broadband results allowed us to identify the processes that produced specific spectral features, while our high-resolution spectra allowed the experimental separation of features that are less than 2 eV apart. We have used the collisional radiative model NOMAD [2] aided by atomic data calculations by FAC [3] to interpret our observations and account for corrections. Experimental results were compared to the atomic database AtomDB, used to fit the galaxy cluster spectra. We found a number of measured features due to DR in lower charge state Ar ions not included in the database, close in energy to the identified line at 3.57 keV, and suggest their inclusion for improved interpretation and diagnosis of other astrophysical spectra.

DEDICATION

To my mother, Belle, and my husband, Deighton for always supporting me.

ACKNOWLEDGMENTS

I would like to thank my advisor and committee chair Dr. Endre Takacs for providing me with so many wonderful opportunities and taking the time sit down and explain things to me. I would also like to thank Roshani Silwal for her support and friendship.

TABLE OF CONTENTS

Page

Table of Contents (Continued) Page

LIST OF TABLES

LIST OF FIGURES

List of Figures (Continued)

Figure Page

List of Figures (Continued)

Figure Page

CHAPTER ONE
INTRODUCTION

The majority of ordinary matter in the universe is in the form of plasma. In astrophysical sources the plasmas vary widely in temperature and electron density from the intergalactic medium at low density (1particle/m^3), to stellar cores of $10^{30}/m^3$ and 10^7 K. We can use the spectra from these objects to gain insights into their physical properties and determine their temperature, density, abundance, and charge distribution.

Astrophysicist often use models to reproduce and understand the spectra from distant sources. A major challenge in using models lies in verifying the accuracy of the results. One field of study, referred to as laboratory astrophysics, aims to selectively recreate the conditions found in astrophysical objects in the laboratory (lab). This allows for the study of specific physical processes by fine-tuning certain parameters such as energy, densities and temperature. These studies can be used to improve the accuracy of the parameters used in the models, such as transition energies, line identifications, oscillator strengths, transition probabilities, etc. [4]. Applying models to the lab measured spectra can also provide verification of the underlying theories used.

This paper describes an experimental investigation of the x-ray spectra of highly charged argon ions, performed at the NIST EBIT for comparison with a model used to fit stacked spectra of galaxy clusters. We begin with the motivation behind our measurements, and then provide some background information on atomic structure, radiative processes, and the devices used in the experiment. Finally the details of the experiment, analysis, and results are provided with some brief conclusions.

1.1 Motivation

Recent studies motivated by the search for a dark matter candidate, the sterile neutrino whose decay may produce an x-ray photon, have reported an unknown x-ray emission feature at 3.55-3.57 keV [1] in the stacked XMM-Newton spectrum of high count galaxy clusters, and at 3.52 ± 0.02 keV [5] in the XMM-Newton spectrum of the Perseus galaxy cluster and the Andromeda galaxy. This possible signature of dark matter has spurred many follow-up studies, some confirming the detection [6,7] while others, including the recent high resolution broadband Hitomi results from the Perseus cluster [8], find little evidence for the unidentified line [9–13]. The existence of the unidentified line is still under investigation and may remain in question until future high resolution x-ray satellite missions measure this energy region in a number of galaxy clusters.

The faintness and close proximity to known atomic transitions brings forth questions of possible non-dark matter related origins of the unidentified feature. Bulbul et al. point out in their report that the feature could be due to a number of atomic transitions [1] including lines from Ar and K, while Gu et al. and Shah et al. make compelling arguments in support of charge exchange between bare sulfur and atomic hydrogen occurring as a result of the interaction between the hot intracluster medium (ICM) and cold dense clouds in galaxy clusters [14,15]. With similar motivations to investigate possible atomic origins of the unidentified line, we used the NIST electron beam ion trap (EBIT) to study the resonant dielectronic recombination (DR) process in Ar XVI, which produces x-ray photons in the energy range of the unknown line. In this

work, measured Ar x-ray spectra are shown that include many DR satellites from lower charge state ions that were not listed in AtomDB, the atomic database often used in astrophysical x-ray spectral modeling.

CHAPTER TWO
ATOMIC STRUCTURE

This chapter provides a short historical introduction along with some basic atomic physics concepts. The concepts provided are summarized from [16] and [17].

2.1 Historical Background and Classical Treatment

Spectroscopy is the study of the interaction between light and matter and it plays an important role in linking fundamental atomic physics to the study of astronomical objects. Spectroscopy is one of the most powerful ways to gather physical information about astrophysical sources and gain insights into their origins and evolution. Isaac Newton, not the first to study spectra, first introduced the term spectra in the 17^{th} century and is typically regarded as the founder of spectroscopy. In his experiments, Newton used a prism to split white light from the sun into its color components and then used a second prism to recombine the constituents back into white light, proving that the colors were actually components of the light and not an artifact created by the prism.

Later in 1814, glass maker Joseph von Fraunhofer invented the first spectroscope, involving a prism, a slit, and a telescope. In his experiments he discovered hundreds of dark lines in the solar spectrum and labeled them alphabetically. Although Fraunhofer did not realize that these dark lines were associated with elements, they are still referred to as Fraunhofer lines and their alphabetic notation continues to be used today. In the 1860's Gustav Kirchhoff and Robert Bunsen were the first to systematically study the spectra of chemical compounds and associate spectral patterns with specific elements. This link

between spectral patterns and elements explained that the dark absorption lines seen in the solar spectrum are due to particular elements. This explanation allowed William and Margaret Huggins to study stellar spectra and discover that stars are made of the same elements found on earth.

Johannes Robert Rydberg, in his study of the spectrum hydrogen and the alkali atoms, was the first to analyze the pattern of emission lines, and in 1888 he formulated the Rydberg formula that explained the observed wavelength of hydrogen emission lines. The Rydberg formula, shown below, gives the wavelength of light λ, where n and n' are whole numbers, and R is the Rydberg constant.

$$\frac{1}{\lambda} = R\left(\frac{1}{n^2} - \frac{1}{n'^2}\right)$$

In 1913 Niels Bohr introduced his theoretical description of the hydrogen atom. By treating the hydrogen atom as an electron moving in a circular orbit around the heavy, stationary, nucleus bound by the Coulomb force, the force balance becomes (in SI units):

$$\frac{m_e v^2}{r} = \frac{e^2}{4\pi\epsilon_0 r^2}$$

Where m_e is the mass of the electron, v is the speed of the electron, r is the radius of the orbit, e the electron charge, and ϵ_0 the permittivity of free space.

Bohr assumed that only certain electron orbits are allowed and that the electron has a different fixed energy in each orbit. When the electron loses energy by jumping between allowed orbits, the atom emits light at given wavelength. The allowed orbits were determined by assuming the quantization of angular momentum, where n is an integer and $\hbar$ is the plank constant over 2π:

$$m_e v r = n\hbar$$

Combining this with the force balance equation above, an expression for the radius of the allowed orbits is found:

$$r = \frac{n^2\hbar^2}{(\frac{e^2}{4\pi\epsilon_0})m_e}$$

The Bohr formula for electron energy using the classical E=T+V is then:

$$E = \frac{1}{2}m_e v^2 - \frac{e^2}{4\pi\epsilon_0 r} = -\frac{e^2}{8\pi\epsilon_0 r} = -\frac{e^2}{8\pi\epsilon_0 a_0 n^2}$$

Where $a_0 = \frac{\hbar^2}{(\frac{e^2}{4\pi\epsilon_0})m_e}$ the Bohr radius, and the integer n is called the principal quantum number.

This theoretical formula for the energy levels of hydrogen reproduces the Rydberg formula that was discovered empirically. While Bohr was coming up with a theoretical model for the hydrogen atom, H. G. J. Moseley was measuring the x-ray spectra of various elements and discovered the empirical relation:

$$\sqrt{f} \propto Z$$

Where Z is the atomic number and f is the frequency of the emitted lines. To mesh the theories together, e^2 in the Bohr formula can be replaced by e^2Z^2. In some cases this replacement produces accurate results for hydrogen-like systems, where the atom has been stripped of all but one of its electrons, giving it a larger nuclear charge than hydrogen, but having the same number of electrons.

For non hydrogen-like atoms, the Bohr formula can be modified by adding scaling factors. This is necessary due to the extra electrons that act to screen the nuclear

charge. For example, if an electron transitions between the n=2 to n=1 shell, the formula can be written as:

$$\frac{1}{\lambda} = R_\infty \left(\frac{(Z-\sigma_K)^2}{1^2} - \frac{(Z-\sigma_L)^2}{2^2} \right)$$

In the equation above, σ_K and σ_L are the screening factor for the n=1 and n=2 shell respectively, and R_∞ is the Rydberg constant. The infinity subscript is used because the nucleus was assumed to be infinitely massive and static. (In some cases the principal quantum numbers are label with letters rather than numbers, starting with K (n=1), L (n=2), M (n=3), and so on alphabetically.)

2.2 Solutions to the Schrodinger Equation.

The classical approach that led to the Bohr model was effective in explaining hydrogen, but failed to accurately describe systems with more than one electron. A more effective method, solving the Schrodinger equation, is outlined here and allows us to expand our treatment to atoms with more than one electron.

The Schrodinger equation for an electron in a spherically symmetric potential is given by:

$$\left\{ -\frac{\hbar^2}{2m_e}\nabla^2 + V(r) \right\} \varphi = E\varphi$$

Where the Laplacian, in spherical coordinates and in terms of the squared orbital angular momentum operator $\boldsymbol{l}^2$, is:

$$\nabla^2 = \frac{1}{r^2}\frac{\partial}{\partial r}\left(r^2 \frac{\partial}{\partial r} \right) - \frac{1}{r^2}\boldsymbol{l}^2$$

The squared orbital angular momentum operator is given by:

$$\boldsymbol{l}^2 = \left\{\frac{1}{\sin(\theta)}\frac{\partial}{\partial\theta}\left(\sin(\theta)\frac{\partial}{\partial\theta}\right) + \frac{1}{sin^2(\theta)}\frac{\partial^2}{\partial\phi^2}\right\}$$

If we separate the wave function into a radial and angular component, $\varphi = R(r)Y(\theta,\phi)$, then we can separate the Schrodinger equation as:

$$\frac{1}{R}\frac{\partial}{\partial r}\left(r^2\frac{\partial}{\partial r}\right) - \frac{2m_e r^2}{\hbar^2}(V(r) - E) = \frac{1}{Y}\boldsymbol{l}^2 Y = \text{b}$$

This equation is true if both sides equal a constant, labeled as b in this case. Now we have an eigenvalue equation: $\boldsymbol{l}^2 Y = b\,Y$. With eigenvalue b and eigenfunctions Y. We can further separate the angular portion of the wave function as $Y(\theta,\phi) = \Theta(\theta)\Phi(\phi)$, then the angular equation becomes:

$$\frac{\sin(\theta)}{\Theta}\frac{\partial}{\partial\theta}\left(\sin(\theta)\frac{\partial\Theta}{\partial\theta}\right) + bsin^2(\theta) = -\frac{1}{\Phi}\frac{\partial^2\Phi}{\partial\phi^2} = m$$

Where again, both sides must be equal to a constant (m), called the magnetic quantum number. The problem on the right hand side of the equation has solutions:

$$\Phi = \text{A}e^{im\phi} + Be^{-im\phi}$$

Imposing the condition that $\Phi(\phi + 2\pi) = \Phi(\phi)$ reveals that m must be an integer, and gives quantization of the magnetic quantum number m. From the definition of the z component of angular momentum operator ${l_z}^2 = -\frac{\partial^2}{\partial\phi^2}$, the eigenvalue problem from above becomes: ${l_z}^2\Phi = \text{m}\Phi$, therefore Φ must be a linear combinations of l_z eigenfunctions.

Since the ladder operators $l_+ and\ l_-$ commute with $\boldsymbol{l}^2$, then Y, l_+Y and l_-Y are all eigenfunction of $\boldsymbol{l}^2$. The raising operator, l_+, raises the z component of the angular

momentum by one unit, transforming the eigenfunction with magnetic quantum number m into another eigenfunction with magnetic quantum number m+1. Similarly, the lowering operator lowers the magnetic quantum number of the angular momentum eigenfunction by one unit. (Definitions of the ladder operators are provided in the Appendix A.1)

There is a limit to how far m can be raised and lowered. Once m has reached its maximum value, applying l_+ will give a zero result. If we call the maximum value $m_{max} = l$, we can find the form of the eigenfunctions as:

$$Y = sin^l\theta e^{il\phi}$$

Substituting this into the Schrodinger equation, we find the eigenvalue b = l(l+1), and we call l the orbital angular momentum quantum number. We can find all of the eigenstates by plugging in m = l into the above equation and applying the lowering operator. For each value of l, m can range from $-l$ to l in interger steps. For example for l = 2, m can be -2,-1,0,1,2. The first few normalized states (spherical harmonics) are given Figure 2. 1 and in general the angular eigenstates are label by their orbital angular momentum and magnetic quantum number $Y_{l,m}$.

$$
\begin{aligned}
Y_{00} &= \frac{1}{\sqrt{4\pi}} \\
Y_{11} &= -\sqrt{\frac{3}{8\pi}}\, e^{i\phi}\, \sin\theta \\
Y_{10} &= \sqrt{\frac{3}{4\pi}}\, \cos\theta \\
Y_{22} &= \sqrt{\frac{15}{32\pi}}\, e^{2i\phi}\, \sin^2\theta \\
Y_{21} &= -\sqrt{\frac{15}{8\pi}}\, e^{i\phi}\, \sin\theta\cos\theta \\
Y_{20} &= \sqrt{\frac{5}{16\pi}}\, (3\cos^2\theta - 1)
\end{aligned}
$$

Figure 2. 1: Normalized Spherical Harmonics

From [18]

Coming back to the separated Schrodinger equation, the radial portion of the equation is now:

$$\frac{1}{R}\frac{\partial}{\partial r}\left(r^2\frac{\partial}{\partial r}\right) - \frac{2m_e r^2}{\hbar^2}(V(r) - E) = b = l(l+1)$$

Using the substitution P = rR(r) gives:

$$-\frac{\hbar^2}{2m_e}\frac{d^2P}{dr} + \left\{\frac{\hbar^2}{2m_e}\frac{l(l+1)}{r^2} - \frac{e^2}{4\pi\epsilon_0 r} - E\right\}P = 0$$

Making the substitution $\rho^2 = \frac{2m_e|E|r^2}{\hbar^2}$ and letting E = -$|E|$ for bound states, the equation then becomes:

$$\frac{d^2P}{d\rho^2} + \left\{-\frac{l(l+1)}{\rho^2} + \frac{\lambda}{\rho} - 1\right\}P = 0$$

Where the coulomb strength is characterized by: $\lambda = \left[\frac{e^2}{4\pi\epsilon_0}\sqrt{\frac{2m_e}{\hbar^2|E|}}\right]$

If we look for a series solution, we get wavefunctions that depend on the principle quantum number n and orbital angular momentum quantum number l, denoted by $R_{n,l}$. The values for l can range from 0 to n-1. A few normalized radial wavefunctions are given in Figure 2. 2.

$$
\begin{aligned}
R_{10} &= 2\left(\frac{Z}{a_0}\right)^{\frac{3}{2}} e^{-Zr/a_0} \\
R_{21} &= \frac{1}{\sqrt{3}}\left(\frac{Z}{2a_0}\right)^{\frac{3}{2}}\left(\frac{Zr}{a_0}\right) e^{-Zr/2a_0} \\
R_{20} &= 2\left(\frac{Z}{2a_0}\right)^{\frac{3}{2}}\left(1-\frac{Zr}{2a_0}\right) e^{-Zr/2a_0} \\
R_{32} &= \frac{2\sqrt{2}}{27\sqrt{5}}\left(\frac{Z}{3a_0}\right)^{\frac{3}{2}}\left(\frac{Zr}{a_0}\right)^2 e^{-Zr/3a_0} \\
R_{31} &= \frac{4\sqrt{2}}{3}\left(\frac{Z}{3a_0}\right)^{\frac{3}{2}}\left(\frac{Zr}{a_0}\right)\left(1-\frac{Zr}{6a_0}\right) e^{-Zr/3a_0} \\
R_{30} &= 2\left(\frac{Z}{3a_0}\right)^{\frac{3}{2}}\left(1-\frac{2Zr}{3a_0}+\frac{2(Zr)^2}{27a_0^2}\right) e^{-Zr/3a_0}
\end{aligned}
$$

Figure 2. 2: Normalized Radial Wavefunctions
From [19]

The energy eigenvalues are then:

$$E = -\frac{2m_e\left(\frac{e^2}{4\pi\epsilon_0}\right)^2}{\hbar^2}\frac{1}{\lambda^2} = -hcR_\infty\frac{1}{n^2}$$

Which is exactly what we found in the Bohr equation. The energy is degenerate with respect to m due to the spatial symmetry, and independent of l due to the nature of the Coulomb potential.

The wavefunctions found represent stationary states, and the electronic charge distribution $e^2|\varphi(r)|^2$ is constant. To study the transitions between the stationary states,

we can examine how an atoms interact with electromagnetic radiation by using an oscillating electric field given by:

$$E(t) = |E_0| Re\left(e^{-i\omega t}\hat{e}_{rad}\right)$$

Where E_0 represents the amplitude of the field, and $\hat{e}_{rad}$ is the polarization vector. If ω is close to the atomic resonance frequency, the electric field induces an oscillating dipole moment on the atom.

The Hamiltonian, H', for the time-dependent interaction between the electric dipole and the electric field E(t) is: $H' = e\boldsymbol{r} \cdot \boldsymbol{E}(t)$. Using time-dependent perturbation theory, the transition rates are approximately given by:

$$Rate \propto |eE_0|^2 \left| \int \varphi_2 * (\boldsymbol{r} \cdot \hat{e}_{rad}) \varphi_1 d^3\boldsymbol{r} \right|^2$$

In Dirac notation: $Rate \propto |eE_0|^2 \times |\langle 2|\boldsymbol{r} \cdot \hat{e}_{rad}|1\rangle|^2$

This can be separated into radial and angular integral components:

$$\left[\int_0^\infty R_{n2,l2}(r)\, r\, R_{n1,l1}(r)\, r^2 dr\right]\left[\int_0^{2\pi}\int_0^{\pi} Y^*_{l2,m2}(\theta,\phi)\hat{r} \cdot \hat{e}_{rad}\, Y_{l1,m1}(\theta,\phi) sin\theta d\theta d\phi\right]$$

The radial integral is not typically zero, and the angular integral typically is zero, unless certain criteria are satisfied. These criteria are called selection rules.

If the unit vector $\hat{r}$ and $\hat{e}_{rad}$ are rewritten in terms of the angular eigenfunctions, then the product becomes:

$$\hat{r} \cdot \hat{e}_{rad} = A_{\sigma-} Y_{1,-1} + A_z Y_{1,0} + A_{\sigma+} Y_{1,1}$$

Where $A_{\sigma-}$ and $A_{\sigma+}$ are the amplitudes of the two circular polarizations in the xy plane (clockwise, and counterclockwise), and A_z *or* A_π depends on the component of the electric field along the z-axis.

Looking at the π transiton for the electric field component along the z-axis, the angular integral becomes

$$Int_\pi = \int_0^{2\pi}\int_0^{\pi} Y^*_{l2,m2}(\theta,\phi)\cos(\theta)\, Y_{l1,m1}(\theta,\phi) sin\theta d\theta d\phi$$

Taking advantage of the symmetry about the z-axis we see that $Int_\pi = e^{i(m_1-m_2)\phi_0} Int_\pi$ leading to $\Delta m_l = 0$ for this transition. For the σ transition, the integral becomes:

$$Int_\sigma = \int_0^{2\pi}\int_0^{\pi} Y^*_{l2,m2}(\theta,\phi)\sin(\theta) e^{i\phi}\, Y_{l1,m1}(\theta,\phi) sin\theta d\theta d\phi$$

Again from symmetry about the z-axis, $Int_\sigma = e^{i(m_1-m_2-1)\phi_0} Int_\sigma$, so that $m_1 - m_2 - 1 = 0$, and the selection rule for σ transitions becomes $\Delta m_l = \pm 1$. If the light is unpolarized then, $\Delta m_l = 0, \pm 1$.

Looking at the angular integral more generally, by replacing $\hat{r}\cdot\hat{e}_{rad}$ with $Y_{1,m}$, the integral becomes:

$$I = \int_0^{2\pi}\int_0^{\pi} Y^*_{l2,m2}(\theta,\phi) Y_{1,m}\, Y_{l1,m1}(\theta,\phi) sin\theta d\theta d\phi$$

Using the relation:

$$Y_{1,m}Y_{l_1,m_1} = AY_{l_1+1,\, m_1+1} + BY_{l_1-1,\, m_1+m}$$

And exploiting the orthogonally of the wavefunctions gives:

$$I = A\delta_{l_2,l_1+1}\delta_{m_2,m_1+m} + B\delta_{l_2,l_1-1}\delta_{m_2,m_1+m}$$

This leads to the previous selection rules, $\Delta m_l = 0, \pm 1$, and an addition rule $\Delta l = \pm 1$.

If we also consider parity symmetry, meaning the energy level structure of an atom should be the same if you take the mirror image since the coulomb potential is the

same when reflected, then the eigenvalues of the parity operator are +1, and -1. When applying the parity operator to our angular eigenfunctions, we get:

$$\hat{P}Y_{l,m} = (-1)^l Y_{l,m}$$

Applying this operator to the eigenfunctions in the angular integral gives:

$$I = (-1)^{l_1+l_2+1} I$$

Since there should be no change to the value of the integral under a parity transformation, an additional constraint is imposed that $\Delta l \neq 0$

2.3 Fine structure

From special relativity we know that if a stationary charge produces an electric field, an observer in a moving frame will experience an electric and magnetic field due to the charge. The magnetic field experienced by a moving electron in an atom can be expressed in terms of its orbital angular momentum:

$$\boldsymbol{B} = \frac{\hbar}{m_e c^2}\left(\frac{1}{er}\frac{\partial V}{\partial r}\right)\boldsymbol{l}$$

The electron has an intrinsic spin angular momentum **s**, of magnitude ½, that produces a magnetic moment given by:

$$\boldsymbol{\mu} = -g_s \mu_B \boldsymbol{s}$$

Where g_s=2, and $\mu_B$is the Bohr magneton = $e\hbar/2m_e$

The Hamiltonian for the interaction between the electron's magnetic moment, and the field is:

$$H = -\boldsymbol{\mu} \cdot \boldsymbol{B}$$

Taking into account the rotating reference frame, Thomas precession, the spin-orbit interaction produces an energy shift of:

$$E_{s-0} = \frac{\beta}{2}(j(j+1) - l(l+1) - s(s+1))$$

Where $\beta = \frac{\hbar}{2m_e c^2}\frac{e^2}{4\pi\epsilon_0}\frac{1}{(na_0)^3 l(l+\frac{1}{2})(l+1)}$ and j = total angular momentum= l+s

A selection rule due to total angular momentum conservation is given as: $\Delta j = 0, \pm 1$.

This somewhat simple approach to spin-orbit coupling is incomplete. There are additional relativistic effects not taken into account. If the relativistic quantum mechanical treatment of the Dirac equation is used, we find that the energy only depends only on n and j, E(n,j). This means that energy levels with the same n and j, but different l have the same energy.

In 1947, Lamb and Retherford measured an energy difference between the $2S_{1/2}$ and the $2P_{1/2}$ states in hydrogen, which was not predicted by the Dirac equation. This energy splitting was later explained with quantum electrodynamics (QED) by Hans Bethe, and the complicated details are omitted here.

2.4. Helium

Solving the Schrodinger equation for Helium becomes complicated and requires a few simplifying assumptions. The Schrodinger equation for two electrons in the coulomb potential of the nucleus is:

$$\left\{\frac{-\hbar^2}{2m}\nabla_1^2 + \frac{-\hbar^2}{2m}\nabla_1^2 + \frac{e^2}{4\pi\epsilon_0}\left(-\frac{Z}{r_1} - \frac{Z}{r_2} + \frac{1}{r_{12}}\right)\right\}\varphi = E\varphi$$

This equation shows that in addition to the coulomb field from the nucleus, the interaction, $1/r_{12}$ term, between the two electrons must be taken into account. The atomic wavefunction can be expressed as a product of wavefunctions for each electron

To solve for an electron in the ground state, and an excited electron in the n,l state, the interaction term is first ignored, and the Schrodinger equation is separated into 2 equations, one for each electron. The wavefunctions for each electron are then:

$$u_{1s}(1) = R_{1s}(r_1) \times \frac{1}{\sqrt{4\pi}}$$

$$u_{nl}(2) = R_{nl}(2) \times Y_{l,m}(\theta, \phi)$$

Treating the spatial part of the atomic wavefunction as $\psi_{space} = u_{1s}(1)u_{nl}(2)$, it is clear that due to the exchange degeneracy, the wavefunction $\psi_{space} = u_{1s}(2)u_{nl}(1)$ will have the same energy.

Treating the interaction term as a perturbation and expressing the atomic wavefunction as a linear combination of the spatial wavefunctions,

$$\psi = au_{1s}(1)u_{nl}(2) + bu_{1s}(2)u_{nl}(1)$$

then multiplying by the complex conjugate and the perturbing term and integrating over space gives coupled equations:

$$\begin{pmatrix} J & K \\ K & J \end{pmatrix} \begin{pmatrix} a \\ b \end{pmatrix} = \Delta E \begin{pmatrix} a \\ b \end{pmatrix}$$

Where J and K are the direct and exchange integral respectively.

$$J = \frac{1}{4\pi\epsilon_0} \int \int |u_{1s}(1)|^2 \frac{e^2}{r_{12}} |u_{nl}(2)|^2 d\boldsymbol{r}_1^3 d\boldsymbol{r}_2^3$$

$$K = \frac{1}{4\pi\epsilon_0} \int \int u_{1s}{}^*(1) u_{nl}{}^*(2) \frac{e^2}{r_{12}} u_{1s}(1) u_{nl}(2) d\boldsymbol{r}_1^3 d\boldsymbol{r}_2^3$$

Solving the eigenvalue equation above gives $\Delta E = J \pm K$, with a=b, and b=-a.
This gives two spatial atomic wavefunctions, one symmetric with energy E+J+K and one antisymmetric with energy E+J-K, where $E=E_1+E_2$ the unperturbed energy of each electron.

$$\psi_{space} = u_{1s}(1)u_{nl}(2) \pm u_{1s}(2)u_{nl}(1)$$

Using the direct and exchange integral and taking electron screening into account, the atomic energies can be found.

The total atomic wavefunction includes both the spin and spatial wavefunction: $\psi = \psi_{space}\psi_{spin}$. Where the spin wavefunctions can also be symmetric or antisymmetric. Since electrons are fermions and must have antisymmetric total wavefunctions with respect to particle exchange, the symmetric spatial wavefunction must associate with the antisymmetric spin wavefunction and vise versa. Another complexity lies in allowed transitions. Unlike in the hydrogen case, an additional selection rule for spin must be applied. In the case of an electric dipole, the operator does not act on spin; therefore the final and initial spin states must be the same since their spin eigenfunctions are orthogonal, $\Delta S = 0$.

2.5 Electron Behavior

Since energy levels depend on the principal quantum number and the total angular momentum, each level can be described by the electron configuration and the term symbol. For light atoms the coupling is weak, so L and S are good quantum number. The spin orbit coupling term symbol used is:

$$^{2S+1}L_J$$

Where S is the total spin, 2S+1 is the multiplicity, L is the total orbital angular momentum, and J is the total angular momentum. Spectroscopic notation is often used for the orbital angular momentum, where S is used for L=1, P (L=1), D (L=3), and so on.

In the previous sections it was noted that for principle quantum number n, the values of the orbital quantum number l range from 0 to n-1, and the magnetic quantum number m range from –l to l. We also know from the Pauli exclusion principal that two or more identical electrons (fermions) cannot have the same set of quantum numbers, or occupy the same quantum state simultaneously. This information helps in determining the electron configuration, which describes how electrons are distributed in atomic orbitals. Each n shell can hold $2n^2$ electrons. The number of electron that can be in a subshell, denoted by l, is 2(2l+1).

For example, the n = 2 shell only allows quantum number l=0,1, m=-1,0,1 and s = +/- ½, this combination of quantum numbers gives 8 different states. For the l=0 subshell m=0 and s = +/- ½, this gives 2 states defined by quantum numbers (n,l,m,s): (2,0,0,1/2) or (2,0,0,-1/2). For the l=1 subshell, m = -1,0,1 and s = +/- ½, leading to 6 independent states: (2,1,1,1/2), (2,1,1,-1/2), (2,1,0,1/2), (2,1,0,-1/2), (2,1,-1,1/2), (2,1,-1,-1/2).
The ground state, or lowest energy term symbol is determined by Hund's rules:
1. For a given configuration, the term with the maximum multiplicity, 2S+1, has the lowest energy.
2. The term with the largest L, total angular momentum, will have the lowest energy.

3. If the outermost subshell is half filled or less than half full, then J, the total angular momentum is the lowest possible value. If it is more than half full, then J is the maximum possible value.

The Aufbau principle allows us to see the ordering for n and l, as shown in Figure 2. 3. For example, an atom with 20 electrons will have an electron configuration of $1s^2 2s^2 2p^6 3s^2 3p^6 4s^2$.

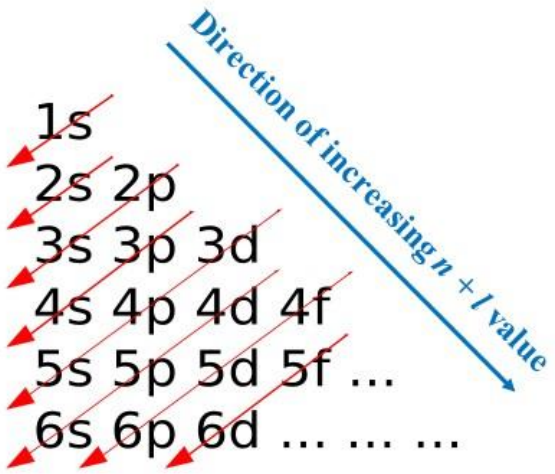

Figure 2. 3: Energy Ordering Rules
From [20]

2.6 Alkalis

Knowing that the electron fill in an order to minimize the energy, we can try to understand why some states seem to fill in a counterintuitive way. For example, why does the 4s shell fill before the 3d? To understand this we can consider the quantum defect effect by looking at the alkalis, elements with filled electron sub-shells except for one unpaired electron.

Recalling the Bohr formula for an electron in a coulomb field, the energy only depends on the principle quantum number. This suggest that the 3d state should have a lower energy than the 4s state. Figure 2. 4 shows the polar plots of the modulus of the angular wavefunctions squared: $|Y(\theta,\phi)|^2$ for hydrogen. Since the electron charge distribution is given as -e$|\psi(r,\theta,\phi)|^2$, the shapes of the $|Y(\theta,\phi)|^2$ plots are related to the charge distribution.

Consider sodium as an example, with a configuration including a closed core, subshell $1s^2 2s^2 2p^6$, and one unbound electron in either the 3s, 3p, or 3d state. The wavefunctions of 3s, 3d, 3p in sodium have a similar shape as those in hydrogen. The d wavefunctions have a single lobe outside of the core and therefore experience screening of the nucleus by the core electrons, having a binding energy similar to hydrogen. The s wavefunction penetrates the core and feels more of the nuclear charge. Since the electron can penetrate the core, there is less screening by the core electrons and consequently the s electrons have a lower energy than d electrons. This is also shown in Figure 2. 5 with the core electrons shaded, and the probability density of the unbound electron shown as a function of r.

To take these effects into consideration, a modified Bohr's formula may be used for alkalis:

$$E(n,l) = -hc\frac{R_\infty}{(n-\delta_l)^2}$$

Where the quantum defect δ_l is given as δ_s=1.35, δ_p=0.86, δ_d=0.01, $\delta_l \cong 0$ for l > 2 for sodium. The quantum defect for other alkalis can be found in tables.

Instead of a quantum defect, the term $n - \delta_l$ can be regarded as the effective principal quantum number, labeled n*.

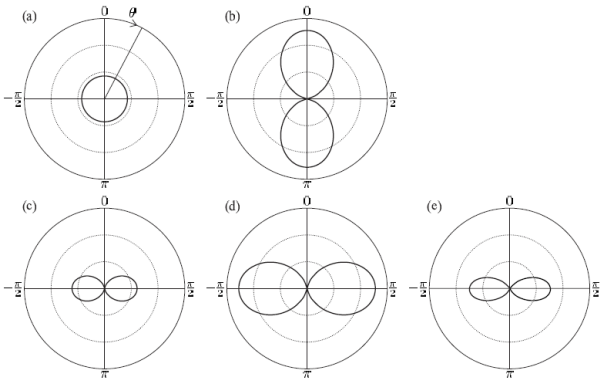

Figure 2. 4: Polar Plots of the Modulus of the Angular Wavefunctions Squared from [16]. a.) $|Y_{0,0}|^2 s\ orbital$, b.) $|Y_{1,0}|^2 p\ orbital$ c.) $|Y_{1,1}|^2$ d.) $|Y_{1,1} + iY_{1,-1}|^2$ e.) $|Y_{2,2}|^2 d\ orbital$

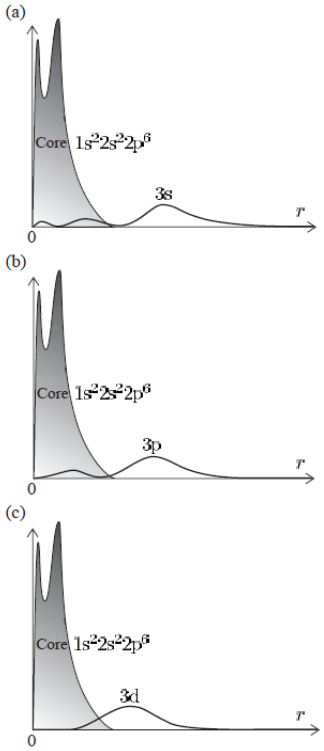

Figure 2. 5: The Probability Density of Electron in Sodium from [16]

2.6.1 Fine Structure Revisited

In the case of the hydrogen atom, the energy difference between fine structure levels was given by:

$$\Delta E_{s-o} = \frac{\alpha^2 hcR_\infty}{n^3 l(l+1)}$$

For alkalis, the energy difference due to fine structure of the valence electron, determined empirically, becomes:

$$\Delta E_{FS} = \frac{Z_i^2 Z_0^2 \alpha^2 hcR_\infty}{n^{*3} l(l+1)}$$

Where $\alpha = \frac{e^2}{4\pi\epsilon_0 \hbar c}$ is the fine structure constant, n* the effective principle quantum number, Z_i the inner atomic number of the atom, and Z_o the outer atomic number outside of the core. This equation, called the Lande formula shows that for hydrogen-like ions with no screening effects, the fine structure scales as Z^4, while for alkalis with heavy screening it scales as Z^2.

2.6.2 Central Field Approximation

Obviously the empirical formulas do not give exact results, and to get a full understanding, all of the electrons must be considered. A central-field approximation can be used to create the following Hamiltonian for N electrons, and used to find the total energy of the atom:

$$H_{CF} = \sum_{i=1}^{N} \left\{ \frac{-\hbar^2}{2m} \nabla_i^2 + V_{CF}(r_i) \right\}, \text{ where } H\psi = E_{atom}\psi$$

Where the central potential includes the coulomb potential from the nucleus and the repulsion between electrons, $V_{CF}(r) = \frac{Ze^2}{4\pi\epsilon_0 r} + S(r)$, and only depends on r.

Assuming V_{CF} applies for each electron, this equation can be separated into N separate equations,

$$\left\{\frac{-\hbar^2}{2m}\nabla_1^2 + V_{CF}(r_1)\right\}\psi_1 = E_1\psi_1$$

and the atomic wavefunction can be expressed as $\psi_{atom} = \psi_1\psi_2\psi_3 \ldots \psi_N$.

The angular momentum is conserved, so the angular wavefunctions are the same $Y_{l,m}$ as in the hydrogen case. The radial equation, using the same P(r)= rR(r) substitution becomes:

$$\left\{-\frac{\hbar^2}{2m}\frac{d^2}{dr} + \frac{\hbar^2}{2m}\frac{l(l+1)}{r^2} + V_{CF}(r)\right\}P = EP$$

To get the form of $V_{CF}(r)$, we can consider the electric field felt by the electron near the nucleus and far from the nucleus. When the electron is close to the nucleus, it can feel the entire nuclear charge, while when it is very far, it only experiences the charge e due to the screening produced by the other electrons. The effective charge experienced by the electron depends on the distance, and the potential can be expressed as:

$$V_{CF}(r) = e\int_{\infty}^{r}\frac{Z_{effective}\,e}{4\pi\epsilon_0 r^2}\,dr$$

This is again an oversimplification since the effect of the outer electron on the other electrons must be considered. To find the energy levels numerical methods are required. A circular procedure must be used since the wavefunction and the potential are unknown. First an estimate of the potential is used to calculate the wavefunctions. The wavefunctions are then used to create a new average potential and new wavefunctions, based on the new potential, are found. The process continues until the results are self-

consistent. To ensure the total wavefunction is antisymmetric, the wavefunction is written as a Slater determinant. This Hartree-Fock method is a standard way of computing wavefunctions.

2.7 Alkaline Earth Metals

Alkaline earth metals, similar to helium, have a closed core and two unbound electrons. To evaluate the spin-orbit interaction in this case, the spin and orbital angular momentum quantum numbers for more than one electron must be considered. For this evaluation first we extend the central field approximation to include a term that represents the part of the electron repulsion not taken into account by the central field, called the residual electrostatic interaction H_{re}, given by:

$$H = H_{CF} + H_{re} = \sum_{i=1}^{N} \left\{ \frac{-\hbar^2}{2m} \nabla_i^2 - \frac{Ze^2}{4\pi\epsilon_0 r} + S(r) + \left(\sum_{j>i}^{N} \frac{e^2}{4\pi\epsilon_0 r_{ij}} - S(r_i) \right) \right\}$$

Finding the wavefunctions and energy solutions is again complicated, and for now we are interested in comparing the strength of the residual term to the spin orbit interaction. For two unpaired electrons the energy shift depends on $L=l_1+l_2$, the total orbital angular momentum, and $S=s_1+s_2$, the total spin angular momentum, rather than the individual electron spin and orbital angular momentum as in the hydrogen case. This LS coupling scheme, with total angular momentum J=L+S, is used when the energy of the residual term, E_{re}, is greater than the spin orbit energy, $E_{s\text{-}o}$.

The spin orbit interaction increases with atomic number, and for heavy atoms the spin orbit interaction may become greater than the residual energy. In high Z elements the electron-nucleus force increases while the electron-electron interaction weakens, and

the velocity of the electron becomes relativistic. In this case the spin orbit interaction is considered before the residual interaction, and l and s couple for each individual electron rather than the total L and S. In this scheme, called jj coupling, the residual terms acts as a perturbation and causes total angular momentum of the electrons to be coupled. This means that l_1 and s_2 couple and l_2, s_2 couple to give j_1 and j_2. The perturbation then causes j_1 and j_2 to couple and the total angular momentum is then $J= j_1+ j_2$.

Figure 2. 6 gives the selection rules for electric dipole transitions in the LS-coupling scheme. The spin orbit interaction splits energy levels with different J values. If an external magnetic field is applied (Zeeman effect), the levels will be further split into levels with different M_J values.

1	$\Delta J = 0, \pm 1$	$(J = 0 \nleftrightarrow J' = 0)$	Level
2	$\Delta M_J = 0, \pm 1$	$(M_J = 0 \nleftrightarrow M_{J'} = 0$ if $\Delta J = 0)$	State
3	Parity changes		Configuration
4	$\Delta l = \pm 1$	One electron jump	Configuration
5	$\Delta L = 0, \pm 1$	$(L = 0 \nleftrightarrow L' = 0)$	Term
6	$\Delta S = 0$		Term

Figure 2. 6: Selection Rules for LS Coupling Scheme from [16]

CHAPTER THREE
RADIATIVE PROCESSES

The brief overviews provided in this chapter are summarized from [17].

3.1 Temperatures

Often we will discuss a temperature of a system. In this context it is assumed that the particles or photons follow an energy or radiation distribution respectively.

The energy of a single particle can be associated with a temperature using:

$$E = h\nu \sim kT \text{ and } E = \frac{1}{2}mv^2 \text{ , leading to: } \frac{1}{2}mv^2 = \frac{3}{2}kT.$$

Typically it is preferred to find the temperature associated with the mean kinetic energy of a system of particles, rather than the temperature of a single particle. In many cases, especially in astrophysics, a Maxwellian speed distribution can be used for particles:

$$f(v) = \frac{4}{\sqrt{\pi}}\left(\frac{m}{2kT}\right)^{3/2} v^2 \exp\left(-\frac{mv^2}{2kT}\right)$$

From this distribution a temperature can be found that best describes the kinetic energies of the system.

For a radiation distribution, often times a blackbody assumption is used. Blackbody objects in thermal equilibrium emit radiation that follows a Plank distribution function:

$$B_\nu(T) = \frac{2h\nu^3}{c^2}\frac{1}{\exp\left(\frac{h\nu}{kT}\right) - 1}$$

Where T in this case represents the radiation temperature of the object, ν is the frequency of the radiation, and B the spectral radiance given in SI units: $W \cdot sr^{-1} \cdot m^{-2} \cdot Hz^{-1}$. From

Figure 3. 1 and Wien's law, the peak of the blackbody spectrum can be used to estimate the temperature.

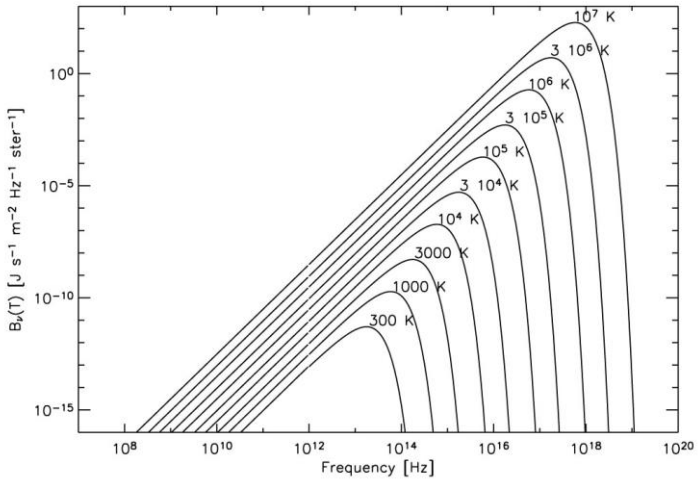

Figure 3. 1: Blackbody Curves

From [21]

3.2 Particles

Electrons, photons, and protons all follow the principle of indistinguishability, meaning they are indistinguishable from other particles of the same type. Fermions, such as electrons and protons, have half integer spins, antisymmetric total wavefunctions that change sign upon switching particle coordinates, and obey Fermi-Dirac statistics. Bosons on the other hand have zero or integer spins, total symmetric wavefunctions that do not change sign upon coordinate switching of two particles, and they obey Bose-Einstein statistics.

As mentioned in the previous chapter, electrons (fermions) with half integer spin must also follow the Pauli Exclusion Principle, meaning no two fermions can occupy the same state or have the same set of quantum numbers. If the temperature of a system of

electrons approaches zero, the electron energies decrease and they must lie in the lowest energy state. Since all electrons cannot occupy the same state, they will occupy the lowest available energy state until the Fermi, highest, level is reached. Following the Fermi-Dirac probability distribution, the number of particles in level N_i is given by:

$$N_i(FD) = \frac{g_i}{exp[(E_i - E_F/kT)] + 1}$$

Where E_i is the energy of level i, E_F is the energy of the Fermi level, k the Boltzmann constant, T the temperature and g_i the statistical weight, or maximum occupancy number, of level i.

As mentioned, Bosons can occupy the same quantum mechanical state. As a result, as the temperature decreases to zero, they can all go into the same low energy state, called a Bose-Einstein condensate. The number of particles in a particular state is given by:

$$N_i(BE) = \frac{g_i}{exp[(E_i/kT)] - 1}$$

In both the Boson and Fermion case, as the temperature increases the distribution approaches the Maxwell-Boltzmann distribution, and the number of particles in level i relative to the total number of particles is given by the Maxwell-Boltzmann distribution:

$$\frac{N_i}{N} = \frac{g_i exp[-(E_i/kT)]}{\sum_j g_j exp\left[-\left(E_j/kT\right)\right]}$$

3.3 Collisional and Radiative Atomic Processes

In general radiative processes may produce characteristic discrete photon energy spectra or they may produce a more continuous energy spectrum. In the next sections, we only consider processes that produce discrete energy spectra.

Chapter two established that the energy levels in atoms are quantized. Now to move on to the interaction of atoms with electromagnetic radiation, we may assume that the radiation field is continuous and not quantized. Einstein first recognized a relationship between absorption and emission by thinking about a simple two energy level (E_1 and E_2) system with statistical weights g_1, and g_2. The transition energy between the two levels is just the difference in energies: $E_{21} = E_2 - E_1 = h\nu$.

Einstein postulated that there are three processes that occur between the two states. 1.) Absorption: a photon with energy $h\nu$ is absorbed from the radiation field ρ. As a result the system transitions from level 1 to level 2 with probability coefficient B_{12}.
2.) Spontaneous Emission: A system in level 2, will drop to level 1 and emit a photon with energy $h\nu$ with probability coefficient A_{21}.
3.) Stimulated Emission: A system in level 2 interacts with a photon of energy $h\nu$, and drops to level 1 and emits a photon of energy $h\nu$ with probability coefficient B_{21}.

When the system is in equilibrium the rate equation shows that population entering 1 equals the population leaving 2:

$$\frac{-dN_2}{dt} = \frac{dN_1}{dt} = A_{21}N_2 - B_{12}\rho_{12}N_1 + B_{21}\rho_{21}N_2$$

Where $B_{12}\rho_{12}$ and $B_{21}\rho_{21}$ represent the transition probability.

In the case of no radiation field, we see that $N_2(t) = N_2(0)\exp(-A_{21}t)$, and that A_{21} gives the lifetime of level 2, and so has units of 1/time.

In the case of steady state, the equation simplifies to:

$$\frac{N_2}{N_1} = \frac{B_{12}\rho(\nu)}{A_{21} + B_{21}\rho(\nu)}$$

Further assuming that the system is in thermodynamics equilibrium, and setting the radiation field equal to the plank function gives the temperature independent Einstein relations:

$$g_1 B_{12} = g_2 B_{21} \quad \text{and} \quad A_{21} = \frac{2h\nu^3}{c^2} B_{21}$$

Since these are temperature independent, these hold even in the case that the system is not in thermodynamic equilibrium. These are also known as detailed balance relations, as they relate a process to its inverse process.

3.3.1 Photoionization and Radiative Recombination

When an atom or ion interacts with a photon it may become ionized or excited. If the energy of the photon is greater than the ionization energy of the bound electron, then the atom may lose an electron and become ionized. The energy of the free electron (ϵ) will be equal to the photon energy ($h\nu$) minus the energy required to free the electron (IE): $\epsilon = h\nu - IE$. This process, called photoionization (PI), can be represented by the equation:

$$X + h\nu \rightarrow X^+ + e(\epsilon)$$

Where X represents a neutral atom, $h\nu$ represents the photon, X+ is the ion, and $e(\epsilon)$ represent the free electron with energy ϵ.

The inverse process of photoionization is called radiative recombination (RR). The RR process occurs when a free electron is captured into a bound state of an ion. The energy lost during the capture is carried away as a photon. This can be described by:

$$X^+ + e(\epsilon) \rightarrow X + h\nu$$

The photon energy in this case is the energy of the free electron E_e plus the binding energy of the capture site: $h\nu = \frac{1}{2}mv^2 + IE$. These processes are shown in Figure 3. 2 where the n=1,2,3 represent the energy levels of the atom/ion and n=∞ represents the bound-free continuum threshold.

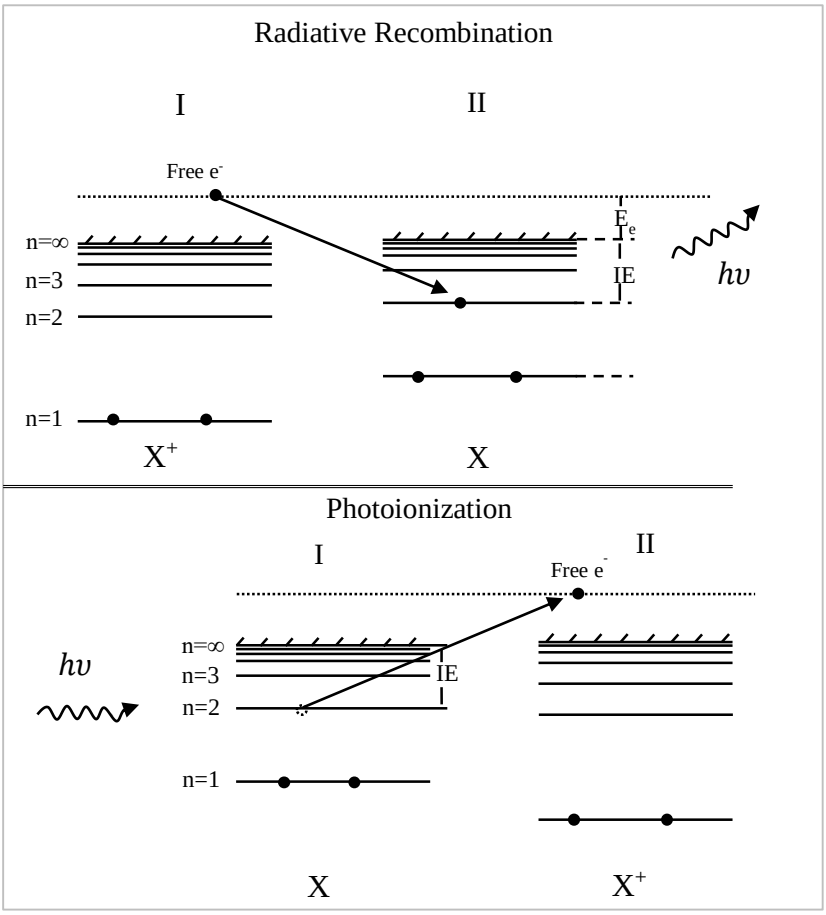

Figure 3. 2: PI and RR Processes

3.3.2 Photo-Excitation and Spontaneous Decay

An atom or ion interacting with photons may absorb a photon with energy $h\nu$, equal to the transition energy between two states (i and j), and excite from state i to state j. Once the lifetime of the transition has been exceeded, the excited atom will spontaneously decay and emit a photon with the same transition energy. The transition probability is given by A as previously described. The photo-excitation and spontaneous emission are shown in Figure 3. 3 and can be described by:

$$X_i^{+n} + h\nu_{ij} \leftrightarrow X_j^{+n}$$

Where X_i^{+n} is an ion with positive charge n in state i, $h\nu_{ij}$ is a photon with energy equal to the transition between states i and j, and X_j^{+n} is the ion with charge n in state j.

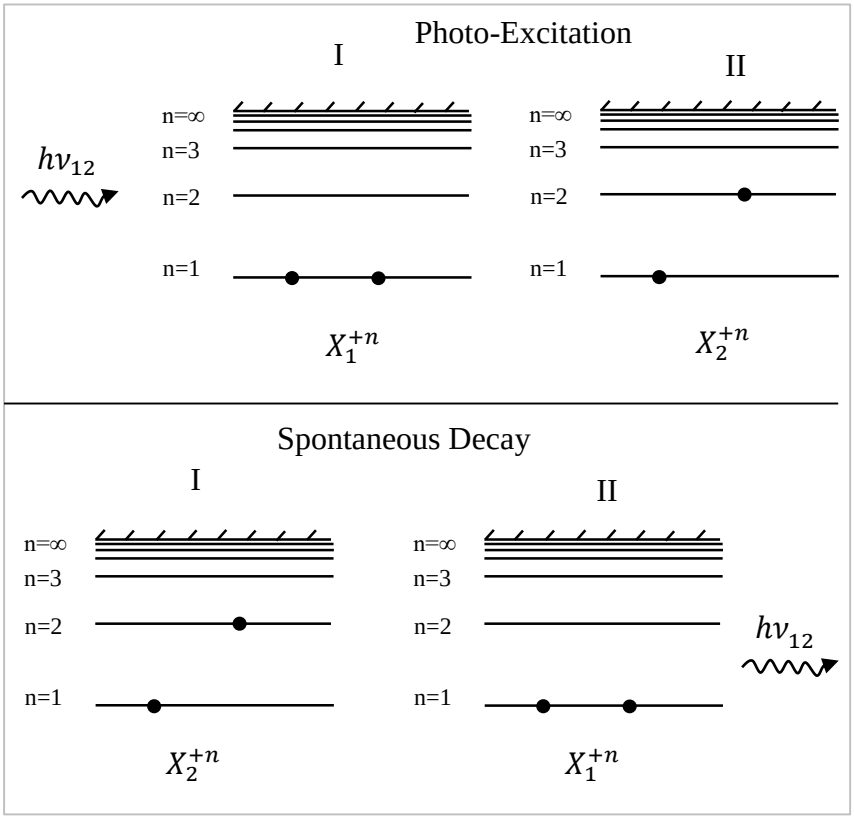

Figure 3. 3: Photo Excitation and Spontaneous Decay Processes

3.3.3 Electron Impact Ionization and Electron Impact Excitation

As shown in Figure 3. 4, an atom may become ionized by interacting with an energetic free electron. If the energy of the free electron (E_{e1}) is greater than the ionization energy (IE) of the bound electron, then the atom may become ionized and the new energy of the initially free electron (E'_{e1}) will be the original energy (Ee1) minus the newly freed electron energy (E_{e2}) minus the binding energy (IE). $E'_{e1} = E_{e1} - E_{e2} - IE$. The reverse process is three-body recombination and involves the collision and recombination of the two free electrons and the ion. The three-body recombination rate is small and not included in Figure 3. 4. These processes are described as:

$$X^{+n} + e(\epsilon) \leftrightarrow X^{+(n+1)} + e(\epsilon') + e(\epsilon'')$$

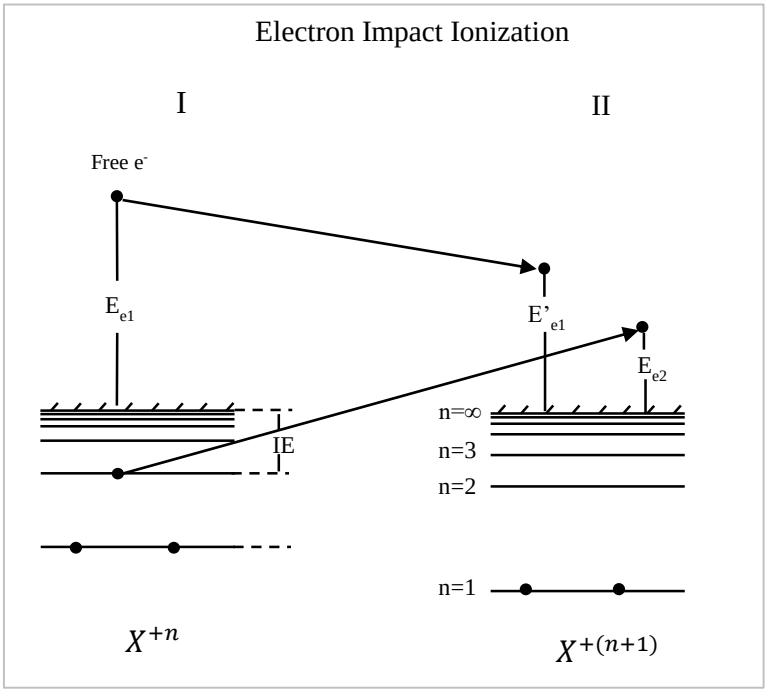

Figure 3. 4: Electron Impact Ionization Process

The electron impact excitation process is shown in Figure 3. 5, where a free electron with energy E($_{e1}$) may excite with an ion, initially in state i, into state j and lose some of its energy (final electron energy E'($_{e1}$)). The excited state then spontaneously decays and emits a photon equal to the transition energy, $h\nu_{12}$. This process is described as:

$$X_i^{+n} + e(\epsilon) \rightarrow X_j^{+n} + e(\epsilon')$$

Where X_i^{+n} is an ion in state i with positive charge n, $e(\epsilon)$ is a free electron with energy ϵ = E($_{e1}$), X_j^{+n} is an ion in excited state j with charge n, and $e(\epsilon')$ is the free electron with lower energy ϵ'= E'($_{e1}$).

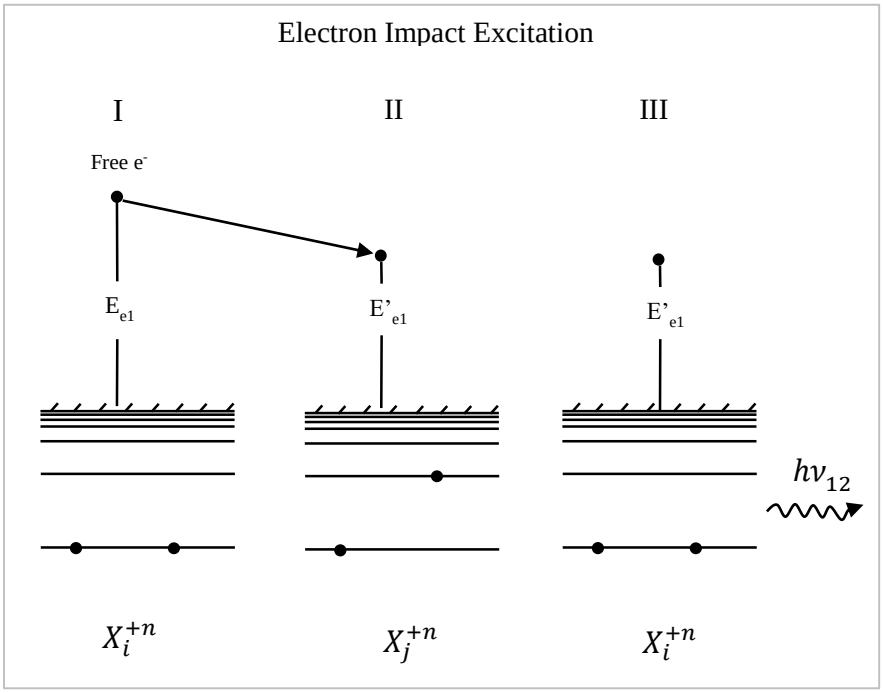

Figure 3. 5: Electron Impact Excitation

3.3.4 Dielectronic Recombination and Autoionization

Since our experiment primarily deals with dielectronic recombination (DR) in highly charged Ar, extra details are included in this section.

Dielectronic recombination is a two-step resonant process by which a free electron is captured into a bound state of an ion while simultaneously exciting an inner shell electron. To complete the DR process one of the excited electrons then spontaneously decays, producing a photon. The DR process can be described by Equation 1, where e^- represent the free electron, X^{+n} an ion (X) with positive charge (+n), $(X^{+n-1})^{**}$ the doubly excited recombined ion with charge (n-1), X^{+n-1} the stabilized ion, and hv the emitted photon energy.

$$e^- + X^{+n} \rightarrow (X^{+n-1})^{**} \rightarrow X^{+n-1} + hv \qquad (1)$$

As seen in Figure 3. 6, autoionization (AI) is a radiationless two step process similar to DR. In the first step of the AI process a free electron is captured into a bound state of an ion while simultaneously exciting an inner shell electron. One of the excited electron spontaneously decays, but rather than producing a photon, the energy is transferred to the second excited electron where it becomes free, leaving the ion in its original charge state, as described below:

$$e^- + X^{+n} \rightarrow (X^{+n-1})^{**} \rightarrow X^{+n} + e^-$$

As an example, the two step KLL DR process in He-like Ar is depicted in Figure 3. 6. The resonant nature of the DR process emerges from the required energy matching of the free electron (E_e) plus binding energy of the capture site (E_b) with the excitation energy (E_2). The photon emitted from the n=2-1 transition in Li-like Ar (Ar^{+15}), is slightly

lower in energy than the analogous transition in the He-like (Ar^{+16}) charge state, and is thusly termed a satellite. The energy difference is attributed to the so called "spectator" electron that shields the nuclear charge. The satellite energy approaches the He-like transition energy threshold as trapped spectator electrons increase in principle quantum number n.

Early theoretical calculations of excitation rates often underestimated the importance of the resonant DR structure and as a result showed poor agreement with experimental results [22]. Later calculations that included resonance features, greatly reduced this discrepancy [23,24]. Accurate excitation rates are important in modeling plasmas as the resonant nature of the DR process produces satellite lines sensitive to plasma temperature. These satellite lines can be more accurate in temperature diagnosis than the often used He-like (w, x, y, z) lines [17]. In particular, the ratio of satellite lines to the He-like resonance (w) line in argon has been identified as an extremely effective temperature diagnostic [25]. The need for accurate DR measurements has led to many EBIT/S measurements of DR resonance strengths and absolute cross-sections. For highly charged Ar these measurements are generally in agreement with theoretical values [26–29].

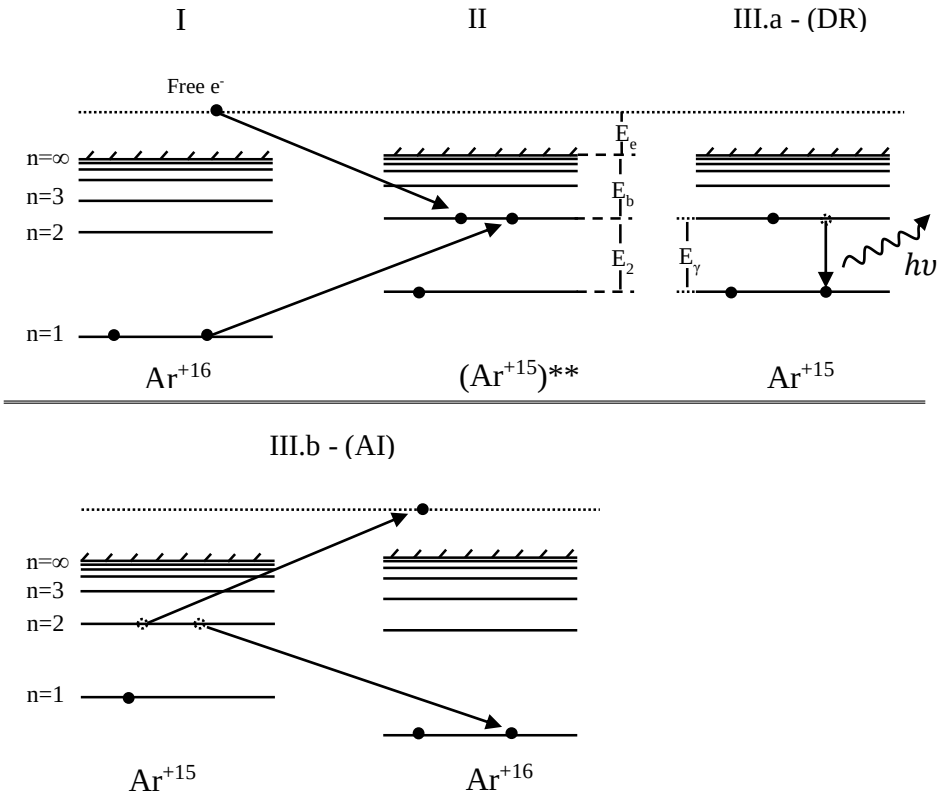

Figure 3. 6: KLL Dielectronic Recombination Process in Highly Charged Argon

I.) He-like Ar ions inside the EBIT trap interact with free electrons in the quasi-mono energetic electron beam. II.) Electrons with resonant energy $E_e = E_2 - E_b$ recombine with He-like ions, lowering the charge state to Li-like, while simultaneously exciting a bound electron, leaving the ion in a doubly excited state. III.a.) The doubly excited state may complete the DR process by stabilizing radiatively, or III.b.) The doubly excited state may autoionize (AI) leaving the ion in the initial He-like charge state.

CHAPTER FOUR
NIST EBIT

This chapter provides a brief description of the Electron Beam Ion Trap (EBIT) located at the National Institute of Standards and Technology (NIST) in Gaithersburg, MD. The NIST EBIT, based on the design of the first EBIT located at Lawrence Livermore Nation Laboratory (LLNL), was designed by Mort Levine in the late 1980s, with the first results published in 1997 [30]. EBITs are relatively small devices that are capable of producing and trapping highly charged ions (HCIs). They have been used for x-ray, EUV, and visible spectroscopic studies of highly charged ions, quantum electrodynamics (QED) studies, and ion-surface studies [31].

4.1 Overview of Ion Production and Trapping

As shown in Figure 4. 1, the NIST EBIT is a vertically oriented device comprised of an electron gun, collector, and drift tube assembly. The electrons, produced by a barium doped 3mm diameter curved cathode, are collimated through the transition electrode and are accelerated towards the drift tube assembly due to the voltage placed on the middle/center drift tube. While traveling, the electrons are compressed into a dense 30μm beam radius by an applied 3T magnetic field. The strong magnetic field peaks in middle drift tube and is produced by a superconducting Helmholtz-pair magnet placed above and below the drift tube assembly. The magnet is kept cool by placing it in contact with a liquid helium reservoir that requires ~3.5 liters of helium per hour [32]. Once the electrons leave the middle drift tube, they spread back out with the magnetic field and are decelerated by the voltage placed on the collector.

Neutral atoms or low charge state ions are injected into the trap region where they undergo successive electron impact ionization. The charge state of the ions can, to some extent, be selected by choosing the appropriate electron beam energy. The variable electron beam energy is quasi-monoenergetic with an energy spread of about 50 eV. Once ionized, the ions are radially trapped by the magnetic field and the potential created by the electron beam. Axial trapping is provided by applying bias voltages to the drift tubes, and will be explained in later sections. The EBIT is kept under vacuum to prevent ions from capturing electrons from the background gas. Once the ions have been created and trapped, spectroscopic studies may be carried out through observation ports located radially around the trap region.

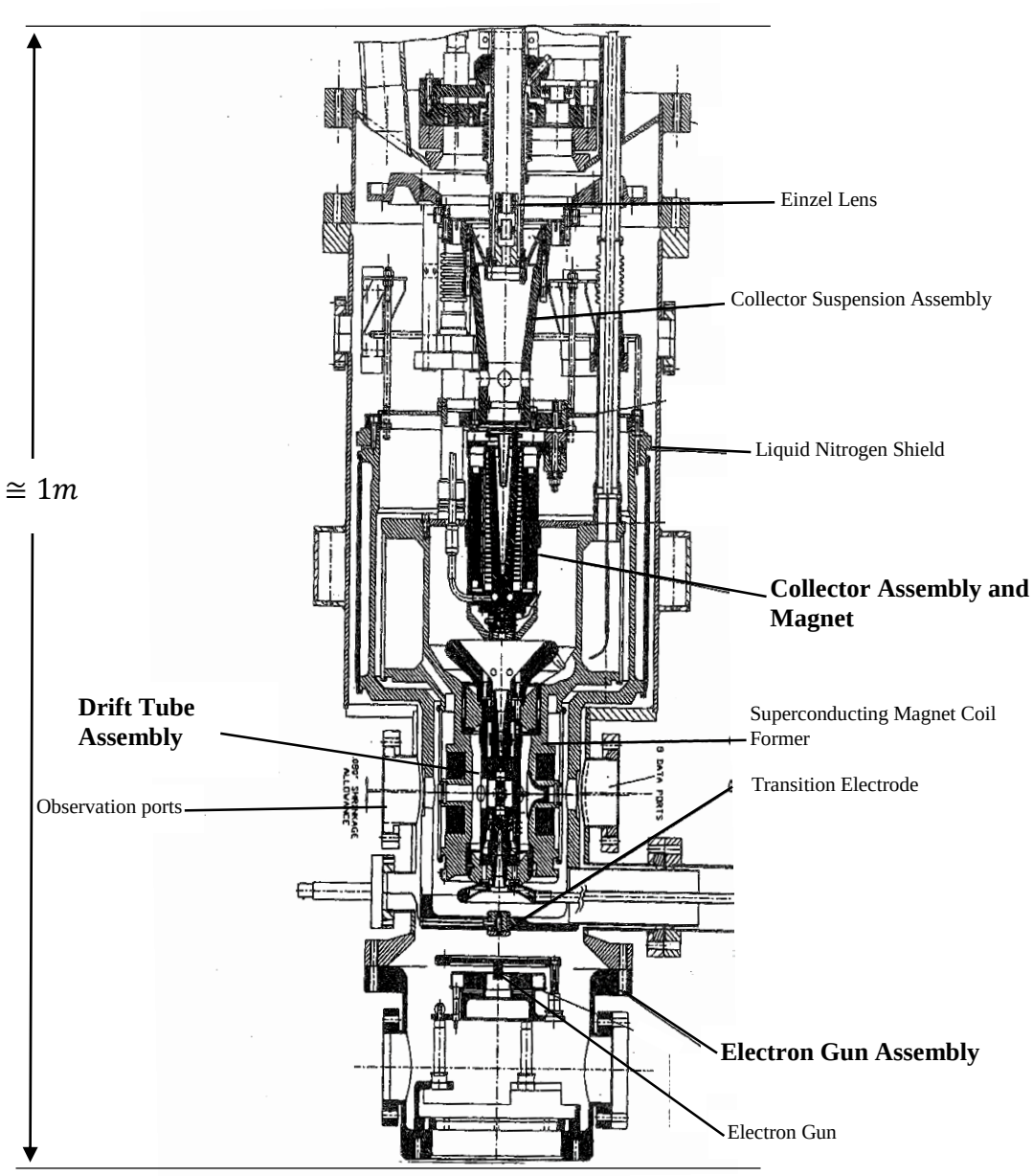

Figure 4. 1:NIST EBIT Drawing from [31], with Added Labels and Dimension

4.2 The Electron Gun Assembly

As shown in Figure 4. 2, the electron gun generally consist of a heater, cathode, focusing elements, anode, snout, shield, and a bucking coil [32] . Electrons are produced from the barium doped 3mm diameter curved cathode. The focus is used to cancel any electrostatic effects created by the cathode so the electrons may move towards the anode. Anode voltage settings control the electron beam current, while the snout is used transition the electrons inside of the assembly to the outside of the electron gun. While the shield is used to block external fields from entering the electron gun assembly, the bucking coil is adjusted to cancel any residual field at the cathode.

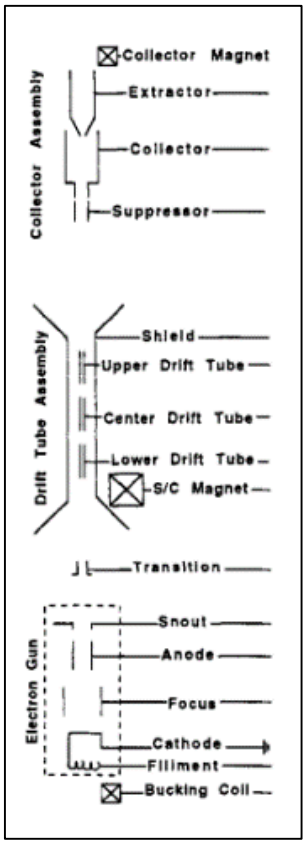

Figure 4. 2: Major EBIT Assemblies, from [30]

According to [32], Chapter 1 by F.J. Currell, the electron beam radius, or the radius through which 80% of the beam passes (r_h) is defined by:

$$r_h = r_b \sqrt{\frac{1}{2} + \frac{1}{2}\sqrt{1 + 4\left(\frac{8kT{r_c}^2}{m\eta^2{r_b}^4B^2} + \frac{{B_c}^2{r_c}^4}{B^2{r_b}^4}\right)}}$$

Where r_b is the radius of the electron beam at the trap, r_c is the cathode radius, kT is the electron temperature at the cathode and the Boltzmann constant, B is the magnetic field at the trap, B_c is the magnetic field at the cathode, η is the electron charge to mass ratio.

This relation shows the importance of the bucking coil, which can be further visualized in Figure 4. 3, showing that as the magnetic field at the cathode is increased, the beam radius increases. Since increased current density is preferred for ion production, a smaller beam radius is desirable and thus a field of zero at the cathode is best.

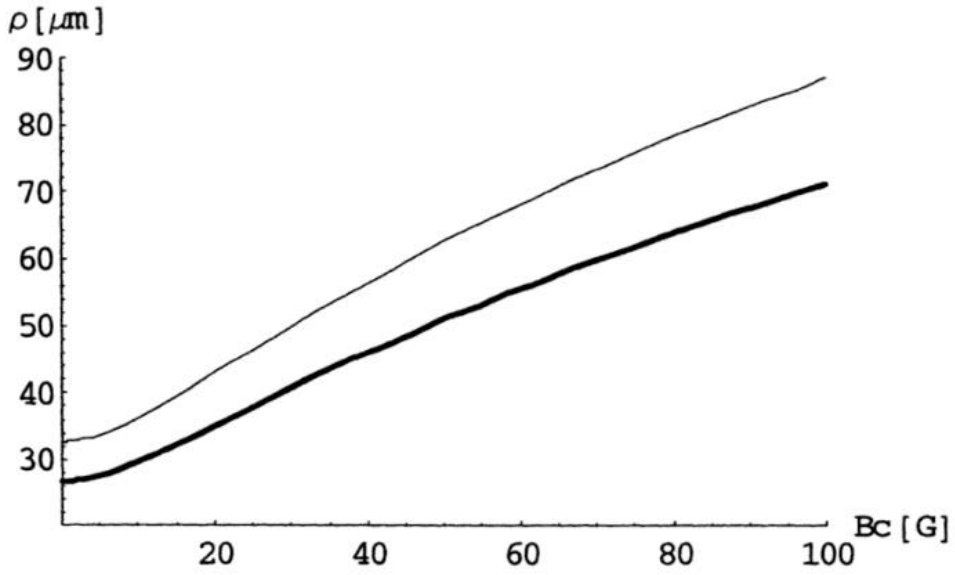

Figure 4. 3 Relation between the Electron Beam Radius and the Field at the Cathode From [32], pg. 16, Figure 6. Thick line is the special case of the Super-EBIT, while the thin line represents general EBITs.

4.3 The Drift Tube Assembly

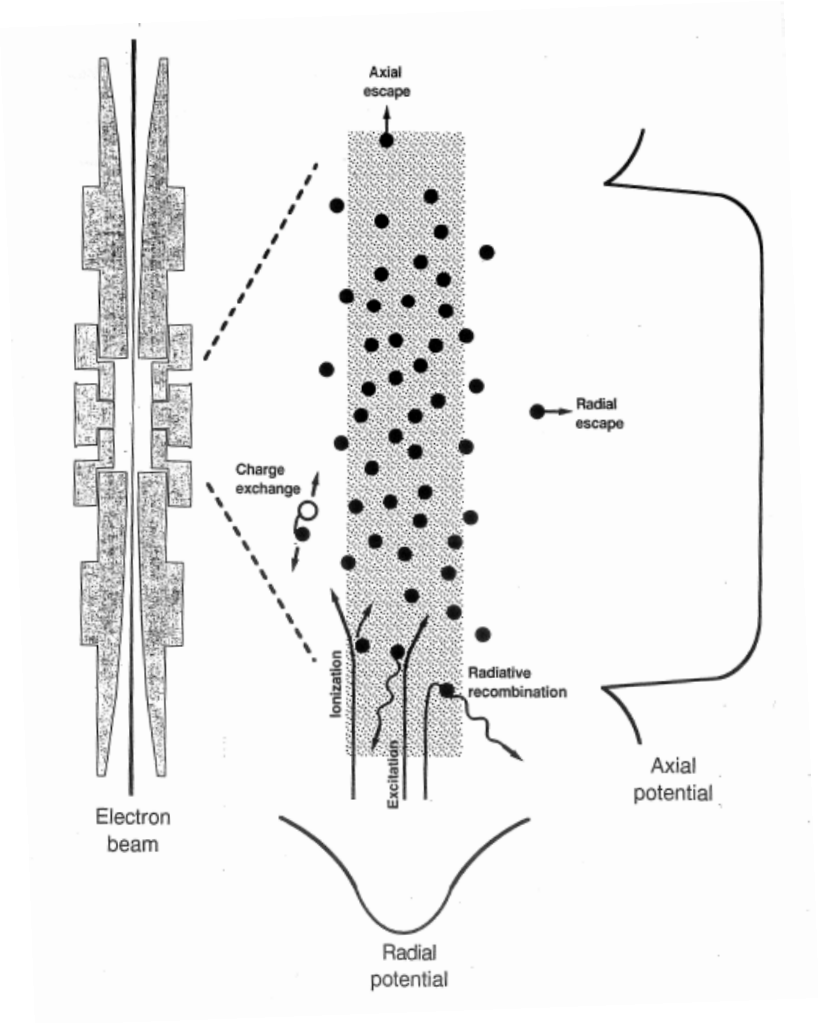

Figure 4. 4: Drift Tube Assembly

From [32], pg. 10, Figure 2, showing (left) drift tube assembly with electron beam running through, and (right) potential traps created with atomic processes occurring between electrons and ions inside of trap. Black dots represent ions.

The drift tube assembly consist of three independent, sequentially aligned, and cylindrical tubes, described in Figure 4. 2 as upper (UDT), lower (LDT), and center drift tube (CDT). The shield surrounding the drift tube assembly is connected to a high voltage power supply capable of producing up to 30 kV, while the lower, center, and upper drift

tubes are controlled by individual power supplies, capable of producing up to 500 V, and can be separately floated on top of the shield voltage. The drift tubes are used to axially trap ions through usage of voltage biases, while the geometry of the drift tubes and electron beam potential radially trap the ions, as seen in Figure 4. 4. When the drift tubes are in trapping mode the center drift tube is typically set to the shield voltage while the upper and lower drift tubes voltages are set a few hundred volts higher than the shield voltage. Periodically the ions are dumped out of the trap by raising the center drift tube voltage above the upper drift tube voltage. Typical voltage settings and times for these two modes are shown Figure 4. 5.

Neutral atoms can be continuously injected into the CDT using a ballistic gas injection system attached to one of the side ports, perpendicular to the electron beam. Atoms not found in gaseous form can be injected, in pulses, as low charge state ions using the metal vapor vacuum arc (MEVVA) ion source on top of the EBIT. The low charge ions are guided into the CDT by spiraling along magnetic field lines.

The energy of the electron beam at the CDT is determined by the sum of the shield voltage and the voltage on the floated CDT power supply. Effects from the potential of the electron beam at the center drift tube wall, also referred to as the space charge, and the potential of the charged ion cloud are also taken into account when calculating the electron beam energy [33]. The total potential at the trap, or center drift tube, is determined by the space charge, the voltage of the CDT, the voltage of the shield, and the potential due to the trapped ions: $V = V_{sc} + V_{cdt} + V_{shield} + V_{ions}$

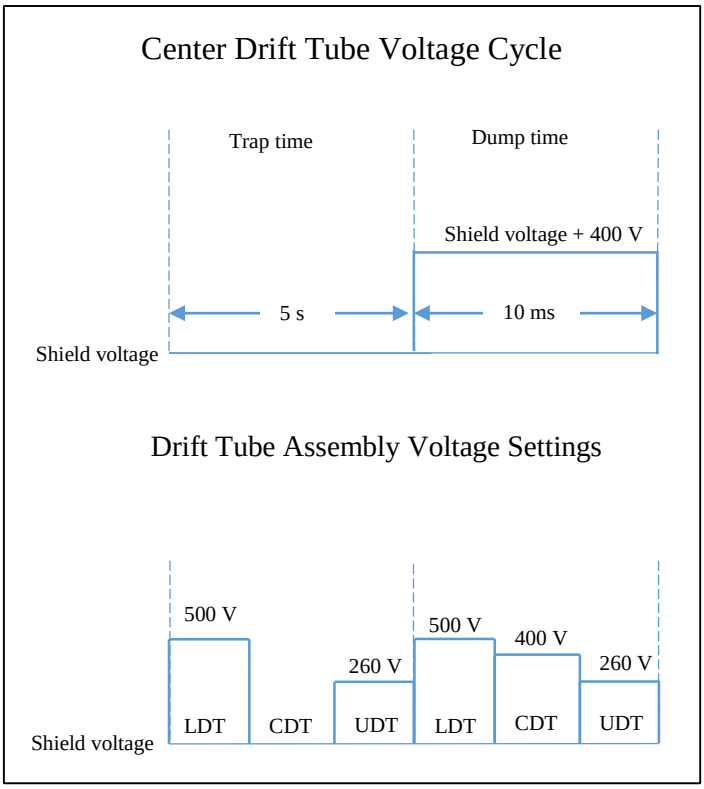

Figure 4. 5: Drift Tube Voltage Cycle

4.3.1 Space Charge Calculation

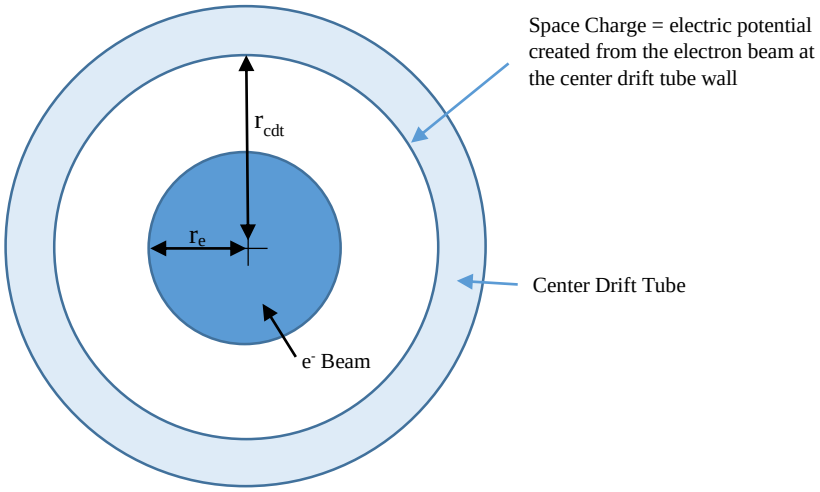

Figure 4. 6 Cross Section through Center Drift Tube and Electron Beam

As previously mentioned, the total potential at the trap dictates the electron beam energy. The potential due to the electron beam will act to raise the applied drift tube voltage and consequently the electron beam energy. For this reason it is important to calculate and correct for this effect.

As shown in Figure 4. 6, taking a cross section through the center drift tube allows us to visualize the electron beam moving through the trap. Treating the electron beam as a long cylinder of charge and using Gauss's law, the electric field outside and inside of the cylinder is:

$$\boldsymbol{E}_{out} = \frac{\lambda}{2\pi r \epsilon_0}\hat{r} \text{ and } \quad \boldsymbol{E}_{in} = \frac{\lambda r}{2\pi {r_e}^2 \epsilon_0}\hat{r}$$

Where λ is charge per unit length, r is the radius of the Gaussian surface, and ϵ_0 is the vacuum permittivity, and r_e is the radius of the electron beam. Integrating the electric field, the potential V_{out} in the region between the electron beam and the center drift tube, where $V_{0,out}$ is a constant, is:

$$V_{out} - V_{0,out} = \frac{\lambda}{2\pi\epsilon_0} ln\left(\frac{r}{r_e}\right)$$

The potential inside V_{in} of the electron beam, from radius 0 to the electron beam radius, with $V_{0,in}$ being constant, is then:

$$V_{in} - V_{0,in} = \frac{\lambda}{4\pi\epsilon_0}\left(\frac{r^2}{{r_e}^2}\right)$$

At r = 0 we can assign the potential $V_{in} = 0$, so $V_{0,in} = 0$.

At the boundary between the region inside and outside of the electron beam ($r = r_e$) the potential should be consistent, $V_{out} = V_{in}$. With this consideration, the constant $V_{0,out}$ is:

$$V_{0,out} = \frac{\lambda}{4\pi\epsilon_0}.$$

The full expression for the radial electric potential of the electron beam, outside of the beam itself is then:

$$V_{out} = \frac{\lambda}{4\pi\epsilon_0} + \frac{\lambda}{2\pi\epsilon_0} ln\left(\frac{r}{r_e}\right)$$

or

$$V_{out} = V_{o,out} + 2V_{0,out} ln\left(\frac{r}{r_e}\right)$$

Using the relation: $\lambda = \frac{I}{v}$ where I is the electron beam current and v is the velocity of the electrons, and the energy relation $= \frac{1}{2}mv^2$, the electric potential can be written as:

$$V_{out} = \frac{I}{4\pi\epsilon_0\sqrt{\frac{2E}{m}}} + \frac{I}{2\pi\epsilon_0\sqrt{\frac{2E}{m}}} ln\left(\frac{r}{r_e}\right)$$

A more accurate description of the electron beam charge distribution may be given by a Gaussian distribution. In this case, we use $V_{0,out} = 1.08\frac{\lambda}{4\pi\epsilon_0}$ [33] and get the following potential relation:

$$V_{out} = \frac{1.08 * I}{4\pi\epsilon_0\sqrt{\frac{2E}{m}}} + \frac{1.08 * I}{2\pi\epsilon_0\sqrt{\frac{2E}{m}}} ln\left(\frac{r}{r_e}\right)$$

To calculate the potential at the center drift tube wall, called the space charge V_{sc}, we use electron beam radius $r_e = 35\mu m$, r = radius of the center drift tube = 5mm, E = electron beam energy at the center drift tube, found from the voltage of the center drift tube, and m= mass of electron. Plotting this potential this at various electron beam

energies and currents, as shown in Figure 4. 7, shows the strong relation between the space charge and electron beam energy.

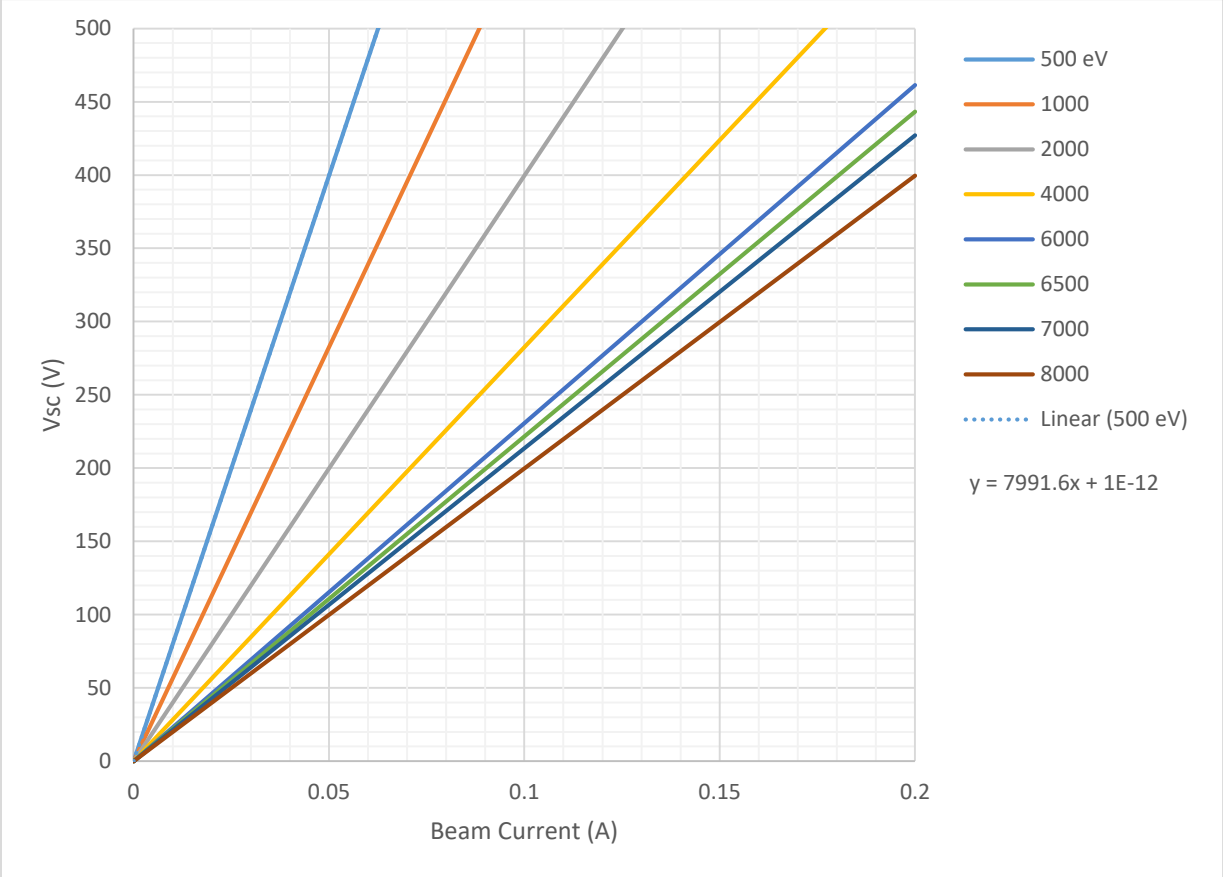

Figure 4. 7: Space Charge Calculated at Various Energies and Currents, With a Linear Trend Line Added to the 500 eV Line

By looking at strong spectral features, measured electron beam energies can be compared to calculated values. The energy difference is attributed to the space charge and neutralization effects caused by the positively charged ions.

4.4 Collector Assembly

As shown in Figure 4. 2, the collector assembly consist of a suppressor, collector, and extractor. The suppressor, situated at the entrance of the collector assembly, acts to repel any electrons created by the bombardment of the electron beam onto the collector. This is achieved by voltage biases, placing a lower voltage on the suppressor electrodes than the collector electrodes. Due to the high current of electrons hitting the collector, some cooling mechanism must be used to cool the collector electrodes. The NIST EBIT utilizes a liquid nitrogen cooling system. The extractor is used to remove ions from the trap and is typically set to a negative voltage to attract positive ions and repel electrons created at the collector.

Typical NIST EBIT parameters used during experiments are provided in Table 4. 1 below.

Table 4. 1: NIST EBIT Parameters

Typical Operating Parameters of the NIST EBIT	
Electron Beam Energy	0.095 keV to 33 keV
Electron Beam Resolution	50 eV
Electron Beam Current	up to 150 mA
Extracted Ion Beam Current (Xe, q= 44+)	> 100 nA (pulsed); > 20 pA (continuous)
Electroun Beam Radius	30 μm
Trap Length	3 cm
Visible Trap Length	2 cm
Number of Ions	> 300000
Ion Density	$3 \times 10^{9}/cm^{3}$
Electron Density	$4 \times 10^{12}/cm^{3}$
Current Density	$5800\ A/cm^{3}$
Vacuum	Below 1×10^{-8} Pa

CHAPTER FIVE
DETECTORS

In this chapter a brief introduction of the basic operating principles of the spectrometer and detectors used during the experiment are outlined. Further details can be found in the references provided.

5.1 Crystal Spectrometer

Early results from the double slit experiment and the photoelectric effect played an important role in establishing the concept of wave-particle duality. The idea that particles can also be treated as waves is clearly shown by De Broglie's formula:

$$\lambda = \frac{h}{p}$$

With h, p, and λ representing the plank constant, particle momentum and wavelength respectively. In the case of massless photons (p=E/c) this relation becomes:

$$\lambda = \frac{hc}{E}$$

With c and E being the speed of light in a vacuum, and the energy of the photon. This relation is useful for going back and forth between photon energy and wavelength.

Studying the spectra of plasma sources is useful in providing physical information about the source, such as the temperature, density, and the elemental abundance. If we consider the resolution of our detector as being the minimum distance between two spectral features that can “just” be distinguished from each other, then it is clear that an increased resolution will provided more accurate information of the source.

Higher resolution devices can allow individual transitions or peaks to be seen in the spectra, while lower resolution devices may blur together many peaks.

One way to spatially "spread out" or disperse the spectra, similar to a prism in the optical wavelength, is to use a spectrometer. Spectrometers may be used for wavelength-dispersion of x-ray photons by taking advantage of Bragg's law. To understand this concept, we can consider a crystal containing planes of atoms that are spaced a distance d apart as show in Figure 5.1. Reference tables typically provide the crystal spacing d, defined parallel to the scattering surface, and the Miller indices (hkl), both values depending on the analyzing crystal and the cut of the crystal.

In general, if an x-ray photon of wavelength λ is incident on the crystal at angle θ, it will be scattered in all directions. If certain conditions are met, namely that (i) the incident and scattered angles are equal and (ii) the rays scattered from different planes are in phase (meaning the path length difference is equal to an integer (n) number of wavelengths), then the scattered photons will constructively interfere and diffraction will occur [34]. Thinking about the second condition it becomes clear that the path length difference between incoming waves 1 and 2 shown in Figure 5.1 is the distance CB + BD=2 CB. From the geometry we can solve for CB using $\sin(\theta) = \frac{CB}{AB}$. The extra path length traveled by wave 2 then is $2\mathrm{AB}\sin(\theta) = 2dsin(\theta)$. Condition (ii) then gives Bragg's law:

$$2\mathrm{d}\sin(\theta) = n\lambda$$

Where θ is called the Bragg angle. This can also be related to the photon energy using the De Broglie formula.

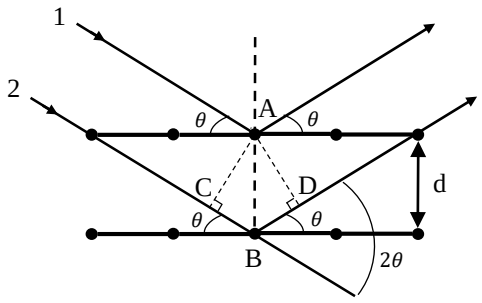

Figure 5.1: Two Photons Incident on a Crystal with Intra Planar Spacing d

Figure 5.1 provides a way to think about flat crystals and shows that the scattered x-rays are not focused. Alternatively, if a curved crystal is used the x-rays will converge to a point or line and can be considered “focused”. Figure 5.2 shows an example of cylindrically curved Johann and Johansson type crystals. The Rowland circle shown is the focusing circle having radius R.

In the Johansson configuration, the crystal is bent to a radius of 2R, and the surface of the crystal is polished to have a radius R matching the Rowland circle, allowing for “perfect” focusing since all points on the crystal are tangent to the Rowland circle. Unlike in the flat case, the angle of incidence does not depend on the angle of the crystal, and all x-rays emanating from a source that satisfy Bragg’s condition will be focused at a point on the Rowland circle, regardless of the placement of the source [35].

The Johann type configuration is simpler in that the crystal is bent to radius 2R and only the axis of the crystal touches and is tangent to the Rowland circle. This is more suitable for crystals that are difficult to polish. The focusing for this case is not as perfect, and may be an issue for small angels, but becomes trivial at large or intermediate

angles [34]. Johann type crystals, similar to Johansson, will also "reflect" same energy x-rays to an area on the Rowland circle, regardless of source placement [35]. When measuring a range of energies, rather than a single energy photon, it is beneficial to place the source inside the Rowland circle, as the angular acceptance increases with the source dimensions that are perpendicular to the direction of the emitted photon [36].

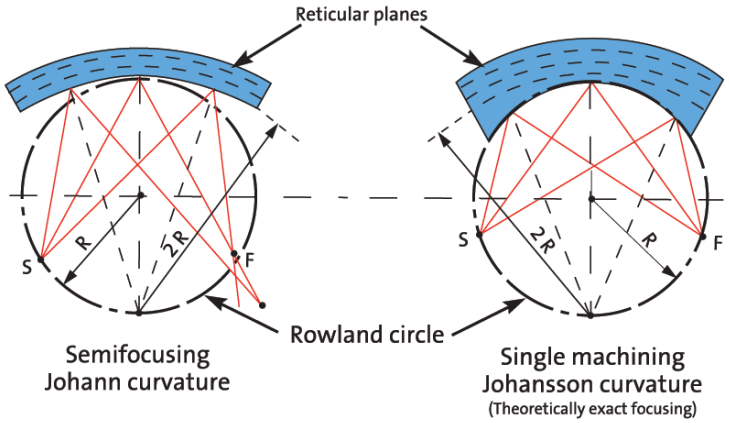

Figure 5.2: Geometrical Description of Johann and Johansson Crystal Configurations Where R is the radius of the Rowland circle, F is the focus, and S is the source location. From [37]

Using the Johann configuration to scatter and focus a single energy photon, ideally the source, crystal, and detector would be on the Rowland circle, with the distance from the source to crystal (L) equal to the distance from the crystal to the detector. From geometry we know the cord length (L) of a circle as $\frac{L}{2} = Rsin(\frac{\emptyset}{2})$. Rearranging to solve for the distance L between two points as shown in Figure 5.3 on the Rowland circle, we get: $L = 2Rsin(\theta)$

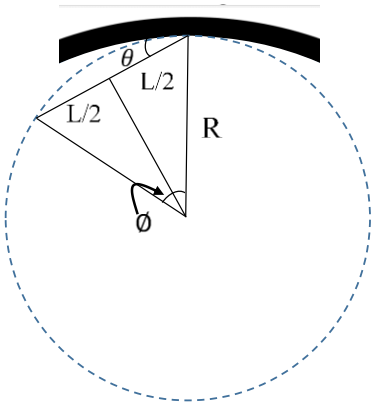

Figure 5.3: Geometry of Rowland circle for a crystal bent to a radius 2R.
Where the length L represents the distance of the source to crystal or crystal to detector.

Therefore, if we know the diameter of the Rowland circle (2R) which in the case of the Johann type is also equal to the radius of curvature of the crystal, we can find the source to crystal or crystal to detector distance for a given Bragg angle.

Knowing the relation for L, devices have been designed for fixed x-ray sources, such as electron beam ion traps (EBITs), that allow the distance from the crystal to the detector to stay constant for varying Bragg angles. The design involves rotating the variable radius crystal and the detector [36]. When a new Bragg angle (energy) is selected, a crystal bender changes the radius of curvature to focus rays onto the detector. This allows L to stay constant by changing R and θ while rotating the detector onto the new Rowland circle, as shown in Figure 5.4.

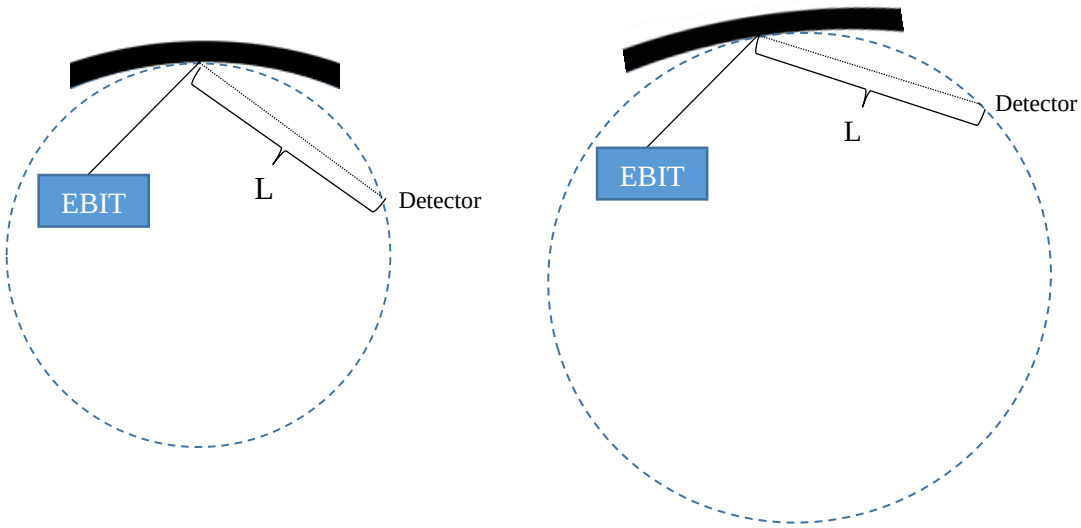

Figure 5.4: Stationary EBIT Source Placed Inside Rowland Circle

Tuning to a different energy changes the position of the crystal and the diameter of the Rowland circle (radius of curvature of the crystal) to keep the crystal to detector distance constant.

Crystal spectrometers can provide high resolution results depending on the energy region of interest, the crystal properties, and the detector. From the differential form of Bragg's law, we see that the dispersion increases as the d spacing of the crystal decreases.

$$\frac{d\theta}{d\lambda} = \frac{n}{2dcos(\theta)}$$

We can also think about this in terms of linear dispersion on a detector plate located tangent to the Rowland circle as shown in Figure 5.5. Using the substitution $dx = Rd\theta$, the linear dispersion equation is:

$$\frac{dx}{d\lambda} = \frac{nR}{2dcos(\theta)}$$

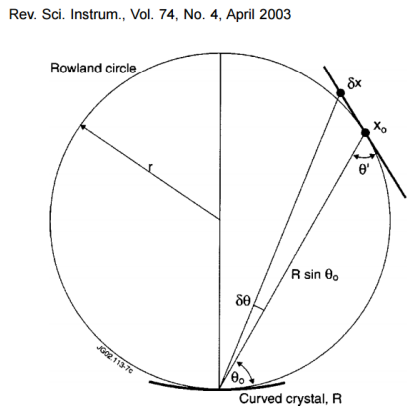

Figure 5.5: Linear Dispersion of a Johann Crystal from [38], Figure 1

As shown in Figure 5.6, large dispersion is good for separating lines close in wavelength, however the measured lines may be broader than the dispersion due to naturally broadening and imperfections of crystal.

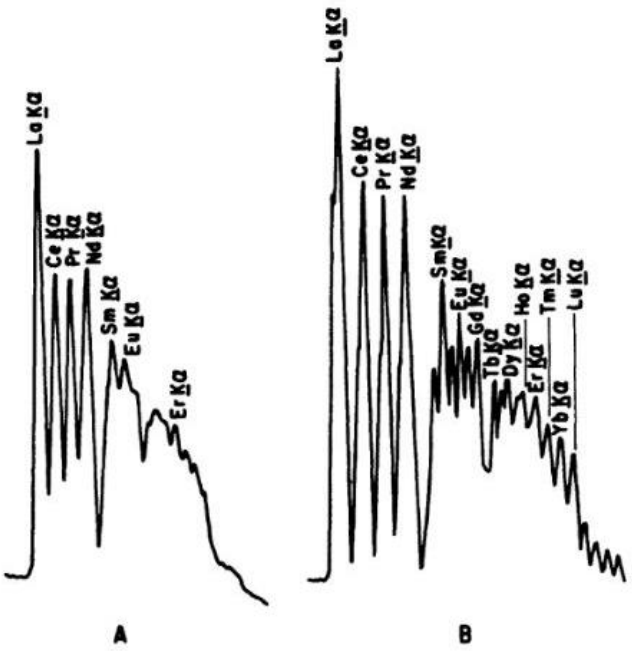

Figure 5.6: Results from Analyzing Crystals with Different 2d Spacing From [34] Figure 5.8. (A) LiF(200) (2d 4.027 Å) (B) LiF (220) (2d 2.848 Å)

We can also use Bragg's law to calculate the resolving power of the spectrometer as:

$$2dsin(\theta) = n\lambda$$

$$2dcos(\theta)d\theta = nd\lambda$$

$$nd\lambda = \frac{2dsin(\theta)}{\lambda}d\lambda$$

$$\cot(\theta)\, d\theta = \frac{\Delta\lambda}{\lambda}$$

For a Johann type crystal the complicated $d\theta$ term includes factors for the detector spatial resolution, the crystal size, index of refraction of the crystal, misalignment, radius setting error, and detector tangent extremity [38]. Typical $\frac{\lambda}{\Delta\lambda}$ values for x-rays can be greater than 3000.

Since detectors are typically limited in size, the more a spectra is dispersed, the less energy/wavelength range is available. The measurable bandwidth depends on the source size, crystal to source distance, the Bragg angle, the radius of the Rowland circle, and the illuminated width of the crystal [38].

Not all photons make it from the source to the detector. The detector efficiency of a Johann type crystal spectrometer depends on the crystal reflectivity, the detector efficiency, the solid angle, the transmission of the observation window (Be), the distance from the source to the crystal, the size of the crystal, size of the detector, and the crystal to detector distance.

5.2 Charge Coupled Devices

Once x-rays have been spatially dispersed by the crystal spectrometer, they need to be detected. One of the best available options for detection is a charge couple device (CCD). CCD's consist of an array of pixels made of silicon. The number of pixels and size of each pixel can vary and are typically limited due to manufacturing limitations. Each pixel is made of a semiconducting material that, upon absorbing an incoming photon, excites previously bound electrons in the valence band of the material into the free flowing conduction band. This leaves "holes" in the valence band, and extra electrons, called photoelectrons, in the conduction band. The free charges created by the incoming photons are collected and trapped using applied voltages. Thermal energy may also excite electrons, which cannot be distinguished from the charges created by photons. For this reason, CCDs are typically cooled to around -75℃ and placed under vacuum to minimize thermal noise. CCD cooling methods include using liquid nitrogen, thermoelectric coolers, or cryo-coolers.

Each pixel has a number of electrodes (gates) attached to it, allowing for a variable potential to be created [39]. The charge is continually collected until the exposure time is over, then the charge from each pixel in a row is simultaneously moved to the next higher row by varying the gate potential as shown in Figure 5.7 A. Charges on the top most row are moved to a row of hidden pixels, that were not exposed to the photons, where they are then dumped into the output electronics one pixel at a time, as shown in Figure 5.7 B.

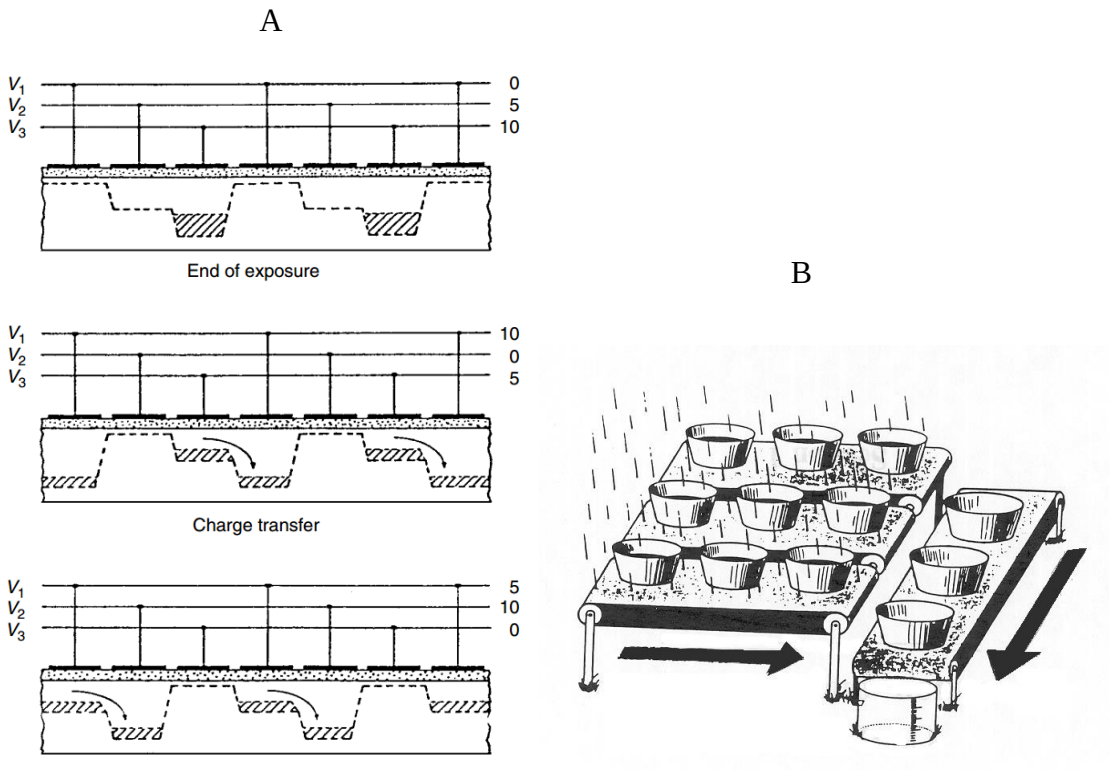

Figure 5.7: CCD Charge Transfer and Collection

A.) Charge transferred from one pixel to the next by varying 3 gate potentials. B.) Charge collected by pixels is depicted as rain drops collected in buckets. Charge is transferred to the top row, then measured one pixel (bucket) at a time. From [39] Fig 2.1 and 2.2.

The charge (or number of electrons) collected is measured as an amplified voltage and is converted into a digital number, called an ADU (analog-to-digital unit), using an analog-to-digital converter. The gain of the CCD is simply the voltage required to produce 1 ADU. The pixel readout process is continued until each pixel has been read and the digital number stored, taking up to minutes to complete. From the ADU readout, a histogram of the counts versus ADU can be used to filter out high ADU cosmic rays or unwanted regions of the spectrum. The positional information can also be used to add

together counts from neighboring pixels from photons that have hit more than one pixel. Finally the ADU can be converted to energy through calibration procedures.

The process explained shows that CCDs work as their own energy dispersion detectors, unlike simple counters. This can be useful when there is a possibility for multiple photon hits in a single pixel during the exposure time. A counter may count a "double hit", two photons hitting a pixel at the same time, as one count. A double hit on a CCD pixel would have double the charge making it easier to identify and either remove or count twice.

As with the crystal spectrometer, not all photons that hit the detector are counted. Some photons pass through the silicon, are reflected, or become absorbed by the gates or some other part of the CCD. Depending on the device, the thickness of the silicon, and the incoming photon energy, the CCD quantum efficiency can be anywhere from a few percent to close to 100%. These values can be found from quantum efficiency curves that are tabulated in literature [39].

5.3 High Purity Germanium Detector

High Purity Germanium (HPGe) detectors are useful for obtaining high count rates in a much shorter amount of time than, for example, the crystal spectrometer. In this description, a Princeton Gamma Tech PRISM 2000 series detector is used to illustrate the basic features and functionality of HPGe detectors.

The most important component of these solid-state detectors are the semiconductor crystal made of high purity germanium that is sensitive to incoming x-ray

photons. The germanium crystal has a p-type and n-type contact, also called electrodes, on each side. Similar to the CCD, incident photons create electron hole pairs, which can be considered as positive and negative charges, in the material that are moved to the appropriate electrode by an electric field (E), as shown in Figure 5.8. The small charge produced enters a charge sensitive preamplifier that creates an output voltage proportional to the integrated input current. Similar to the CCD, the voltage pulse height is proportional to the energy of the photon, and according to the Princeton Gamma Tech detector manual, an incoming photon of 2.96 eV produces one electron-hole pair.

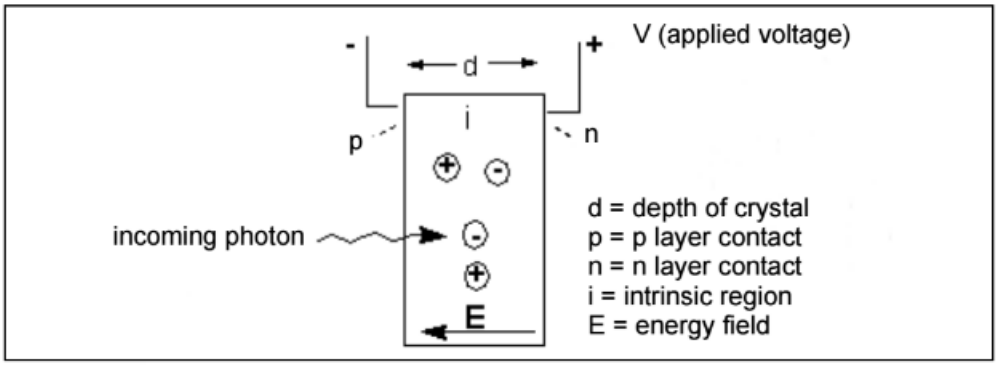

Figure 5.8: Charge Production Process
From the Princeton Gamma Tech PRISM 2000 Series Detector Manual (2001), Figure 4.1.

In the Princton Gamma Tech schematic shown in Figure 5.9, prior to hitting the detector, photons pass through a thin beryllium window that separate the detector from the source. (X-rays are able to pass through beryllium without being absorbed due to its low density and atomic mass.) This allows for x-ray measurements while the source is placed under vacuum. Once the photon hits the HPGe crystal, cooled by liquid nitrogen, the small charge that has been created by the incoming photon travels to the field effect

transistor (FET) for signal amplification. Each photon hit, or event, takes some time to be processed. Any new event that occurs while the previous event is being processed is ignored, as such this is called the dead time. Once the current signal has been converted into a voltage, a histogram of the counts per pulse height or energy can be created. The bins or channels can then be converted to energy by calibration and the spectrum is created.

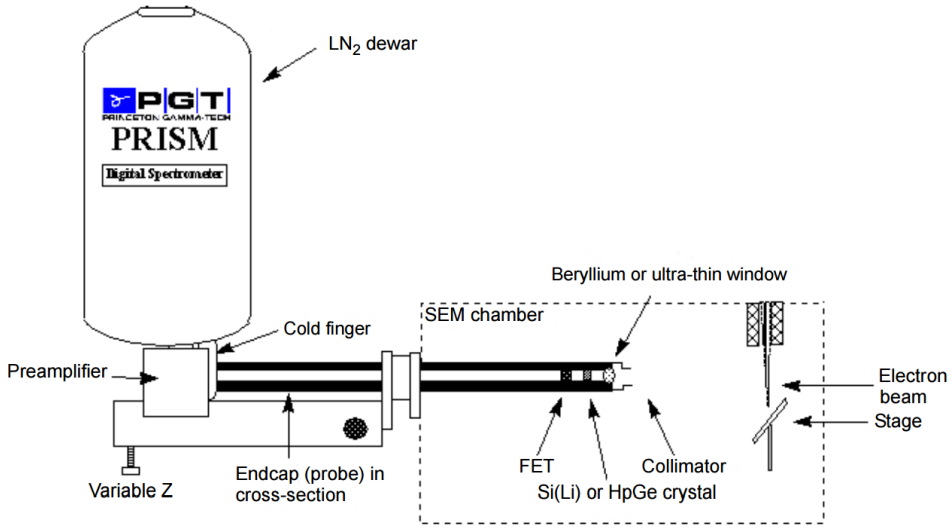

Figure 5.9: Schematic of an HpGe Detector used in Tandem with a Scanning Electron Microscope (SEM)

From the Princeton Gamma Tech PRISM 2000 Series Detector Manual (2001).

4.2. Resolution:

There are many factors that affect the energy resolution of the germanium detector. If we simplify things and only consider the effects of statistical fluctuations and electronics noise, the energy resolution can be written as:

$$(\Delta E_{measured})^2 = (\Delta E_{statistical})^2 + (\Delta E_{E\ noise})^2$$

The statistical fluctuation in converting photon energy into charge carriers, for semiconductor detectors is given as full width at half maximum (FWHM) [40] by:

$$\Delta E_{statistical}(\text{FWHM}) = 2.35\sqrt{FE\epsilon}$$

Where F is the Fano factor, E the photon energy, and ϵ the conversion factor from photon energy to number of charge carriers (2.96 eV produces one electron-hole pair for HPGe detector). The resolution due to electronics noise is given as:

$$\Delta E_{E\ noise} = 2.35(ENC)\epsilon/q$$

Where q is the electron charge, and ENC is the equivalent noise charge. The ENC depends on the electronic components being used and the temperature. As such it is important to keep the detector cool to reduce the ENC.

CHAPTER SIX
EXPERIMENT AND ANALYSIS

6.1 Experiment

Aimed at producing and studying He-like argon, x-ray spectra of highly charged argon ions were measured at the electron beam ion trap (EBIT) facility located at the National Institute of Standards and Technology (NIST) over a 4 day period. Details of the operating principles of the EBIT and detectors used can be found in previous chapters and references.

To prepare our system, neutral argon atoms were continuously injected into the center drift tube at an optimized pressure of approximately 2.5E-5 Torr. The electron beam current was set to 60 mA while the shield voltage, controlled by labView or by directly changing the power supply, was initially set to 2.2 kV, well above the ionization threshold of Li-like Ar (918.374 eV). The trap voltage cycle included a charge breeding time (cooking time) of 5 s during which the upper (UDT) and lower (LDT) drift tubes were set to a higher positive voltage than the center drift tube (CDT). This was followed by a 10 ms dumping time during which the CDT voltage was raised above the UDT voltage (but lower than the LDT) to remove any buildup of contaminants. Usual contaminant species are barium ions that emanate from the electron gun.

Pressures, voltages, currents, and resistances were recorded for EBIT components on each day that measurements were taken, and are given in Table 6. 1. Values that did not change from day to day are only listed for Day 1.

To improve statistics, measurements were taken in a “steady state” mode, where the electron beam energy remains constant during data acquisition. In this mode, the plasma is in equilibrium at each electron beam energy setting, and the charge state balance will vary with electron beam energy. This requires modeling of the EBIT to determine the charge state balance at each beam energy. The models used, which include the flexible atomic code (FAC) and NOMAD, have proven successful in producing accurate EBIT spectra in earlier experiments [41–43]

Table 6. 1 EBIT Parameter on Each Day of Measurements

Parameter	Day 1	Day 2	Day 3	Day 4
Beam Line Pressure (Torr)	1.44E-09	1.53E-09	1.99E-09	1.94E-09
E- Gun Pressure (Torr)	1.40E-10	1.00E-10	1.00E-10	1.40E-10
Crystal Spectrometer (Torr)	2.60E-03	1.20E-05	1.10E-05	1.10E-05
Gas Injection Pressure (Torr)	4.34E-09	1.88E-08	2.30E-08	2.16E-08
Super Magnet Resistance (Ohm)	5.8	3.00E-02	0.00E+00	2.40E-02
Focus (V)	-8.39			
Suppressor (V)	620			
Einzel Lens (V)	1500			
Extractor (V)	-2180			
Transition (V)	5.36			
Filament (V)	6.3			
Filament (Amp)	0.482			
TC1 (Collector Exhaust) °F	315			
Upper Drift Tube (V)	260			
Lower Drift Tube (V)	500			
Middle Drift Tube (V)	400			
Collector Magnet Voltage (V)	5			
Collector Magnet Current (A)	0.5478			
SC Magnet Current (A)	147.7			
Bucking Coil Voltage (V)	0.53709			
Snout (mA)	< 15			
Collector Voltage (2kv)	2			

The shield voltage/electron beam energy was scanned from 2.2 kV to 5.2 kV in 15V steps to identify all of the DR resonances. X-rays were collected for 3 minutes while scanning the beam energy, and for 15 minutes at the resonance energies. Once resonance peaks were identified, the gas injection pressure was varied at the resonance energy of interest to maximize the count rate, as shown in Figure 6. 1.

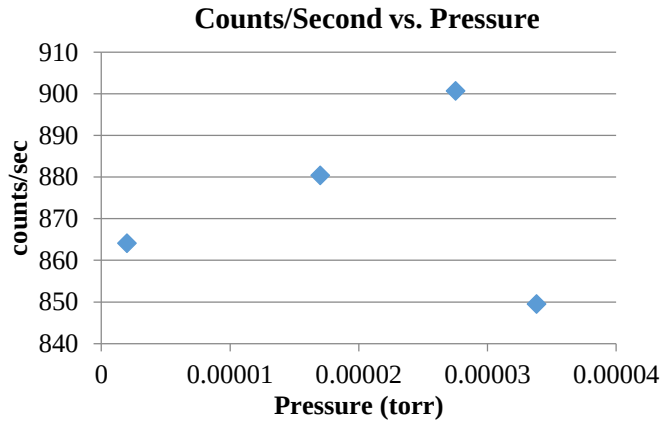

Figure 6. 1: Pressure Optimization Measurements

A Canberra LN_2 cooled high purity Ge (HPGe) detector and an Andor ikon-L CCD detector attached to a Johann-type crystal spectrometer were used to take x-ray measurements at the EBIT observation ports. The HPGe detector was separated from the EBIT through a 340 nm thick aluminum-coated polymer window The crystal spectrometer was housed with a Si (111) crystal, with a spectral range of 2.219 to 4.592 keV and a 2d spacing of 6.271 Å [44], and was separated from the EBIT vacuum by a 230 μm thick Beryllium window. The 2048 x 2048 pixel array CCD was cooled to -75 °C using chilled water, the readout rate was 50 KHz with a 4x amplification, and the images

were saved in .sif and .fits format. The camera was kept at a vacuum level of 2.6 $x10^{-3}$ torr and the data was collected using single data acquisition mode. During data acquisition, the pressure gauge was turned off to enhance the signal to noise ratio. The hardware temperature is maintained by the camera software ANDOR Solis.

6.2 Analysis and Results

6.2.1 Broadband Results

The surface plot shown in Figure 6. 2, resulting from HPGe spectra taken at multiple electron beam energies, highlight some of the charge state altering atomic processes occurring inside the EBIT. (Calibration procedure used for HPGe detector can be found in Appendix B). Ions excited by the quasi-monoenergetic electrons from the beam through electron impact excitation emit one or many photons upon stabilization. This process preserves the charge state of the ion and produces the intense vertical lines seen in Figure 6. 2. Unbound electrons may also radiatively recombine (RR) with ions, mostly into the n= 2 and 3 states for He-like Ar, and emit a photon equal to the ionization energy of the capture site plus the energy of the free electron. The single capture RR process leaves the ion in a once lower charge state and produces the diagonal lines seen in Figure 6. 2. As previously described, the resonant DR process only occurs when the energy of the free electron plus the ionization energy of the capture site in the one lower charge state matches the inner shell excitation energy. This resonant process produces the intense spots in Figure 6. 2. Additional features due to DR and RR processes in barium ions emanating from the barium oxide coated cathode of the electron gun are seen as diagonal lines and bright spots between 4000 and 8000 eV in Figure 6. 2.

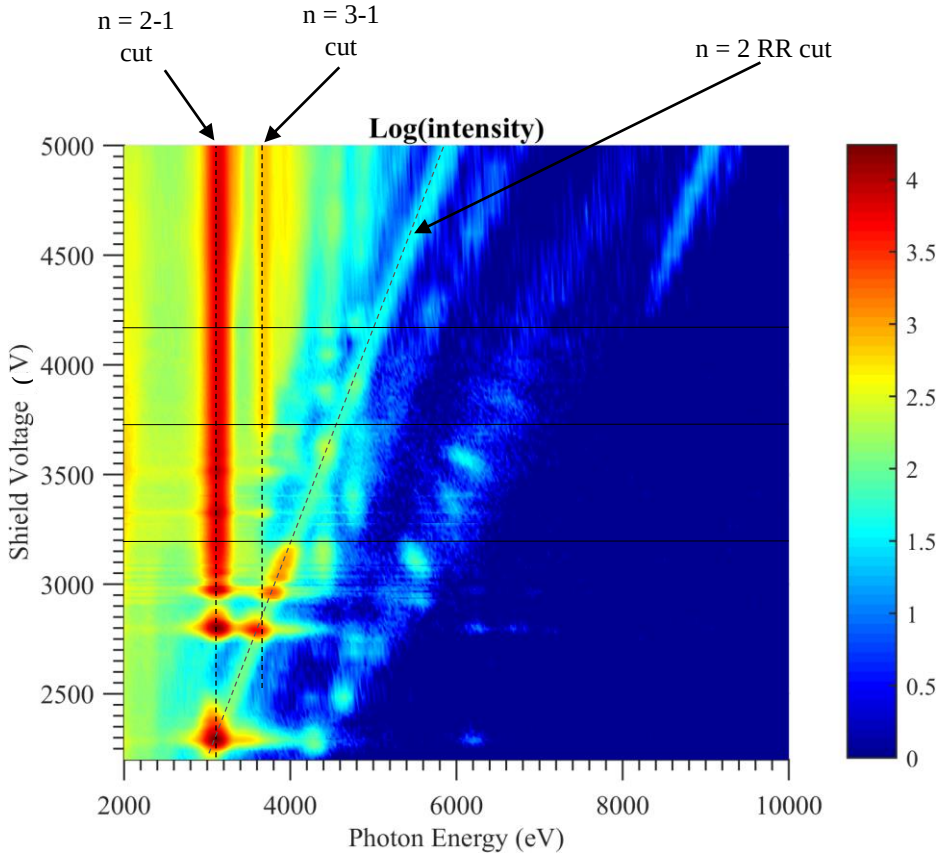

Figure 6. 2 Surface plot from HPGe measured photon intensities and energies at electron beam energies between 2500 and 5000 eV

To scan over all of the Li-like Ar DR resonances, spectra were taken with shield voltage settings between 2.15 kV and 5.15 kV with 15 V increments. Slices taken down the n=2-1 and n=3-1 direct excitation (DE) lines, and through the diagonal n=2 radiative recombination (RR) line in Figure 6. 2 were collapsed onto the vertical axis. To make the direct excitation cuts, the spectra above the DE threshold and at the resonance were studied to estimate the energy width of the DE peak. A Matlab code, found in the Appendix-A.1, was created to add up all counts within that energy range at each electron beam energy (shield voltage) and then the sum of counts were plotted versus the shield

voltage. A similar procedure was used for the radiative recombination cut, however for each data point the energy range was shifted by the change in electron beam energy. Results are shown in Figure 6. 3.

He-like Ar DE thresholds were found from the transition energies listed in the NIST Database as 3139.58 eV for the 1s2p to ground state, and 3683.848 eV for the 1s3p to ground state transition. The He-like ionization energy for the ground state was listed in the NIST Database as 4120.6655 eV. The DE threshold and ionization energies were estimated in shield voltage by plugging in shield voltage values into a space charge calculator created in Microsoft excel. The calculator is used to convert shield voltage into electron beam energy by taking into account space charge and ion cloud neutralization effects. By reversing the calculation, the shield voltage that produces a given energy can be found.

The threshold values have also been added to the contour plot (Figure 6. 2) for further emphasis. The DR resonances are labeled in Figure 6. 3 using a common 3 letter notation, with the first, second, and third letter representing the shell of the initial unexcited bound electron, the shell of the excited electron, and the capture site shell of the recombined electron respectively.

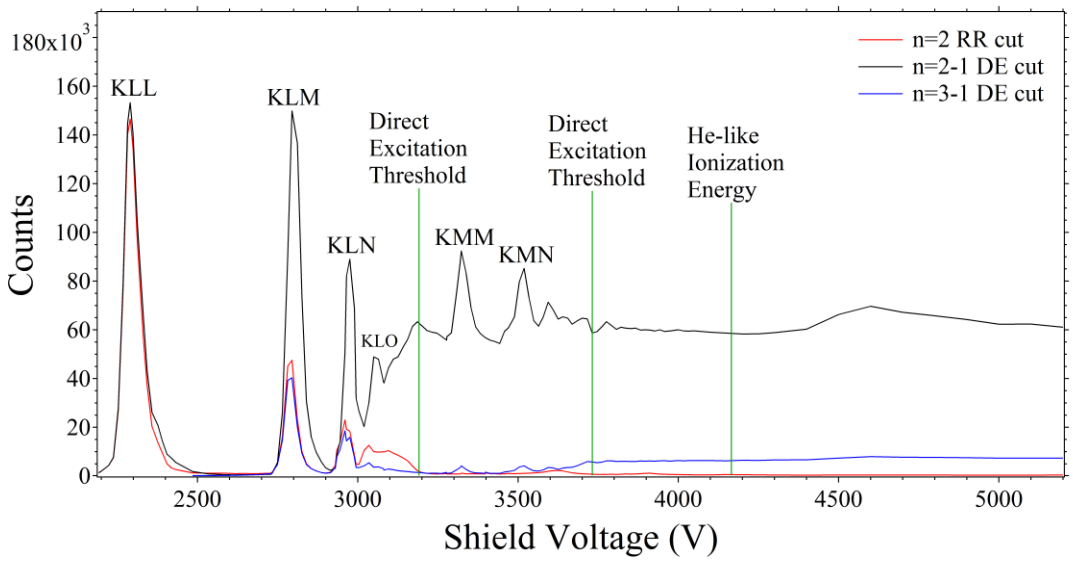

Figure 6. 3 Cuts From HPGe Surface Plot

Plot created from HPGe spectrum of Li-like Ar DR Resonances at shield voltages between 2.15 and 5.15 kV. Black: $1s^2nl'$-1s2lnl' transition. Blue: $1s^2nl'$-1s3lnl'. Red: radiative recombination to the n=2 shell.

6.2.2 High Resolution Results

Argon spectra taken with a high-resolution crystal spectrometer at an electron beam energy corresponding to a maximum intensity of the KLM resonance is shown in Figure 6. 4. Measurements were taken for five consecutive three minute intervals, then added to improve the signal to noise ratio. The fine structure of the n=2-1 transition, with spectator electron at n = 3, in Li-like Ar is seen between 3100 and 3150 eV, while the n=3-1 transitions, with spectator at n=2, is seen between 3600 and 3650 eV.

Additional spectra of He-like Ar, taken at electron beam energies away from DR resonances, were used with NIST tabulated values of the well-known He-like w,x,y, and z lines to calibrate the spectra. From the calibrated spectrum shown in Figure 6. 4, an

additional Ar feature was identified around 3560 eV, very close in energy to the reported unidentified line.

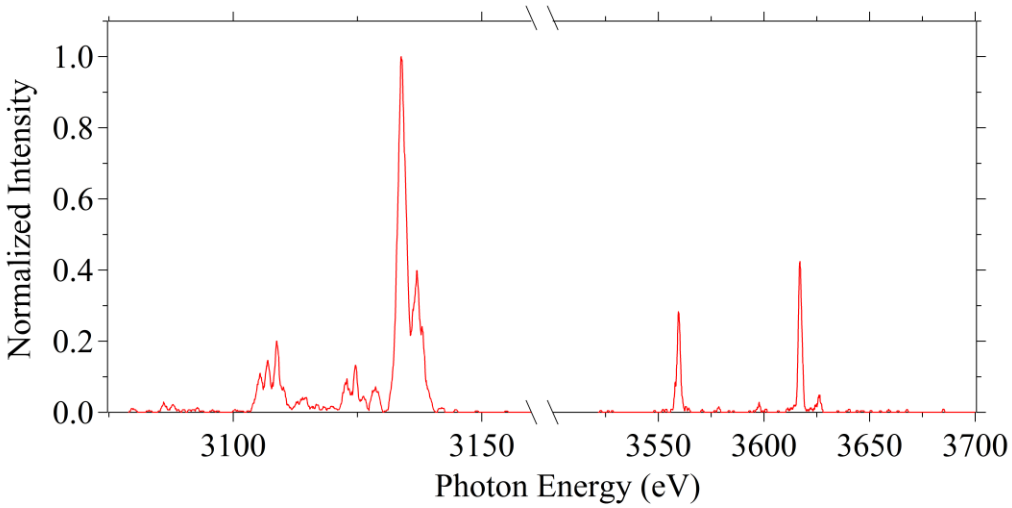

Figure 6. 4: Measured Ar EBIT Spectra

6.2.3 Comparison with Modeling

To understand the charge state balance and correctly identify measured lines, we compare our measured spectra to calculated spectra. We used the flexible atomic code (FAC) [3] to calculate atomic structure, transition rates, and collisional cross section data. The non-maxwellian collisional radiative package NOMAD [2] was used to calculate level populations and line intensities, including contributions from charge exchange, at each electron beam energy.

Since three minute measurements were taken at each electron beam energy, the ion charge distribution is considered to be in steady state. Using the rate equations we find the density of neutral atoms (n_0) in the interaction region to be our only free parameter. Evaluating the ratio of the RR peaks of H-like and bare Ar in the spectra at

higher, off-resonance, electron beam energies we were able to accurately determine the number of neutrals and produce calculated spectra and surface plots.

Figure 6. 5 shows the theoretical surface plot convolved with a typical HPGe detector response. Measured features including the intense DR spots, direct excitation, and RR lines are clearly replicated, verifying our model of the charge state distribution at each electron beam energy. The theoretical high resolution spectra, taken at an electron beam energy corresponding to the maximum intensity of the KLM resonance, is shown in Figure 6. 6. Measured lines of Figure 6. 4 are reproduced, including the interesting line around 3560 eV. The calculated line identifications revealed that this feature results from $1s^2 2s2p$-$1s2s2p3p$ electric dipole DR transitions in Be-like Ar.

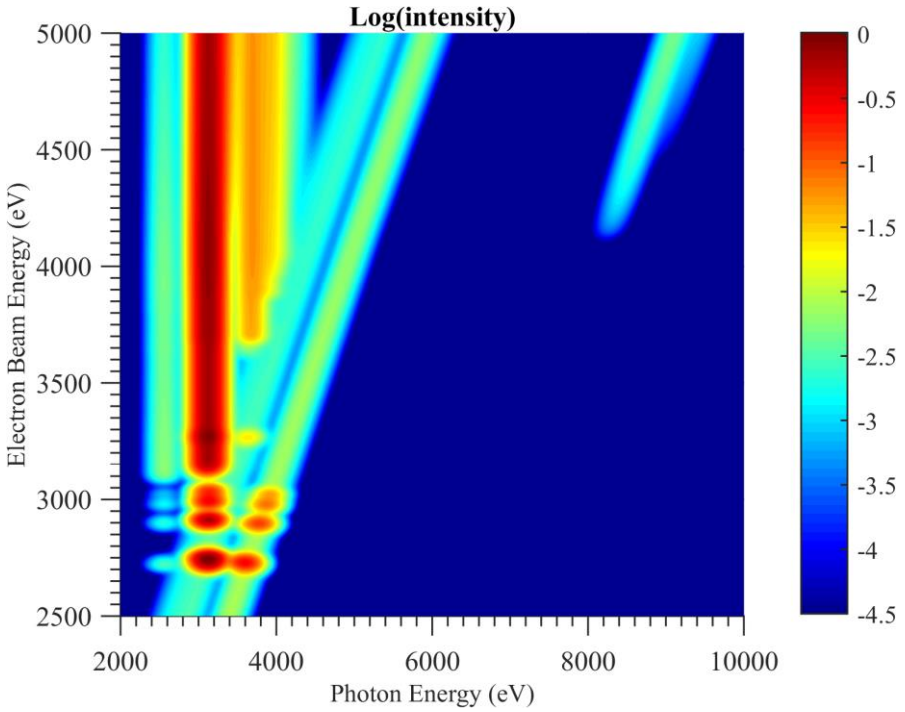

Figure 6. 5: Surface plot Calculated Using NOMAD and FAC

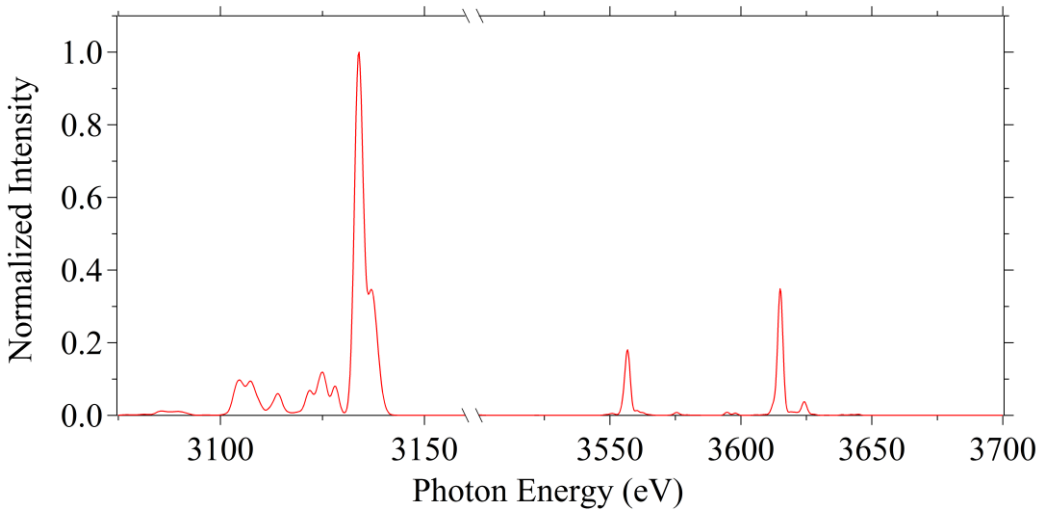

Figure 6. 6: Calculated Ar EBIT Spectra

6.3 Comparison with the Atomic Database

The astrophysical atomic database AtomDB was used in the analysis of the stacked spectra of galaxy clusters [1]. Strong Ar emission lines were fit to the cluster spectra along with a few weaker lines, including the mentioned Li-like Ar DR satellite lines listed in AtomDB at an energy of 3.618 and 3.617 keV and relative intensities of 0.39 and 1 respectively. Though these two lines are not fully resolved even in our measured high-resolution spectra, we do see the blended line in Figure 6. 4. The Ar XV DR line measured around 3560 eV has an intensity comparable to the two Ar XVI DR satellite lines at 3.618 and 3.617 keV; however the Ar XV DR line was not found in the atomic database, AtomDB. Further inspection revealed that indeed, only a few low charge state DR lines are listed in the database.

6.3.1 Case of a Maxwellian Plasma

The EBIT ions are produced and excited by a semi-monoenergetic electron beam, producing a non-maxwellian plasma; however, the hot intracluster medium of galaxy clusters, responsible for producing the majority of the emission, is assumed to follow a Maxwellian distribution. To investigate the importance of the measured lower charge state Ar XV line emission feature, the Ar spectra of a Maxwellian distributed plasma was calculated using FAC and NOMAD at temperatures between 250 and 3500 eV. Figure 6. 7 shows the intensities, plotted on a log scale, along with the photon energy and input temperature. As shown in Figure 6. 8, the 3.56 keV Ar XV line intensity was plotted versus the plasma temperature, revealing that the line feature is most prominent between 750-1000 eV.

The FAC/NOMAD calculated spectra at 1000 eV shown in Figure 6. 9 was used to identify strong features, and additional information about the labeled transitions can be found the Appendix A.3-Table A. 1. These calculated lines were compared to the listed lines in AtomDB, as shown in Figure 6. 10. The AtomDB lines were obtain by using the online WebGUIDE and searching for lines between 3 and 4 keV. There were 77 Ar lines listed, whereas there were 200 lines calculated by FAC. The FAC calculated lines are color coded by charge state, whereas the AtomDB listed lines are all given in red.

Zooming into the energy region of interest around 3560 eV, as done in Figure 6. 11, shows that many Li-like and Be-like Ar DR satellite lines are missing from the database. It is worth noting that the lines listed in AtomDB are provided for the temperature that gives the maximum emissivity. This means that not all of the lines listed

are at 1000 ev like the FAC lines. This makes it difficult to compare the line intensitites from FAC to emissivities given in AtomDB, and is the reason intensities were not provided on the verticle axis.

The importance of lower charge state ions in galaxy clusters were discussed recently by groups who argue that charge exchange may be a contributing source of the unknown emission feature [14,45]. If charge exchange between cold clouds and the hot intracluster medium or any other contributing processes are producing lower charge state ions, then we argue that the emission from these low charge state ions may be more important than previously thought. Additionally, the low charge state emission may be blended with more dominant lines leading to overestimates of strong lines within the galaxy cluster spectral emission feature fits.

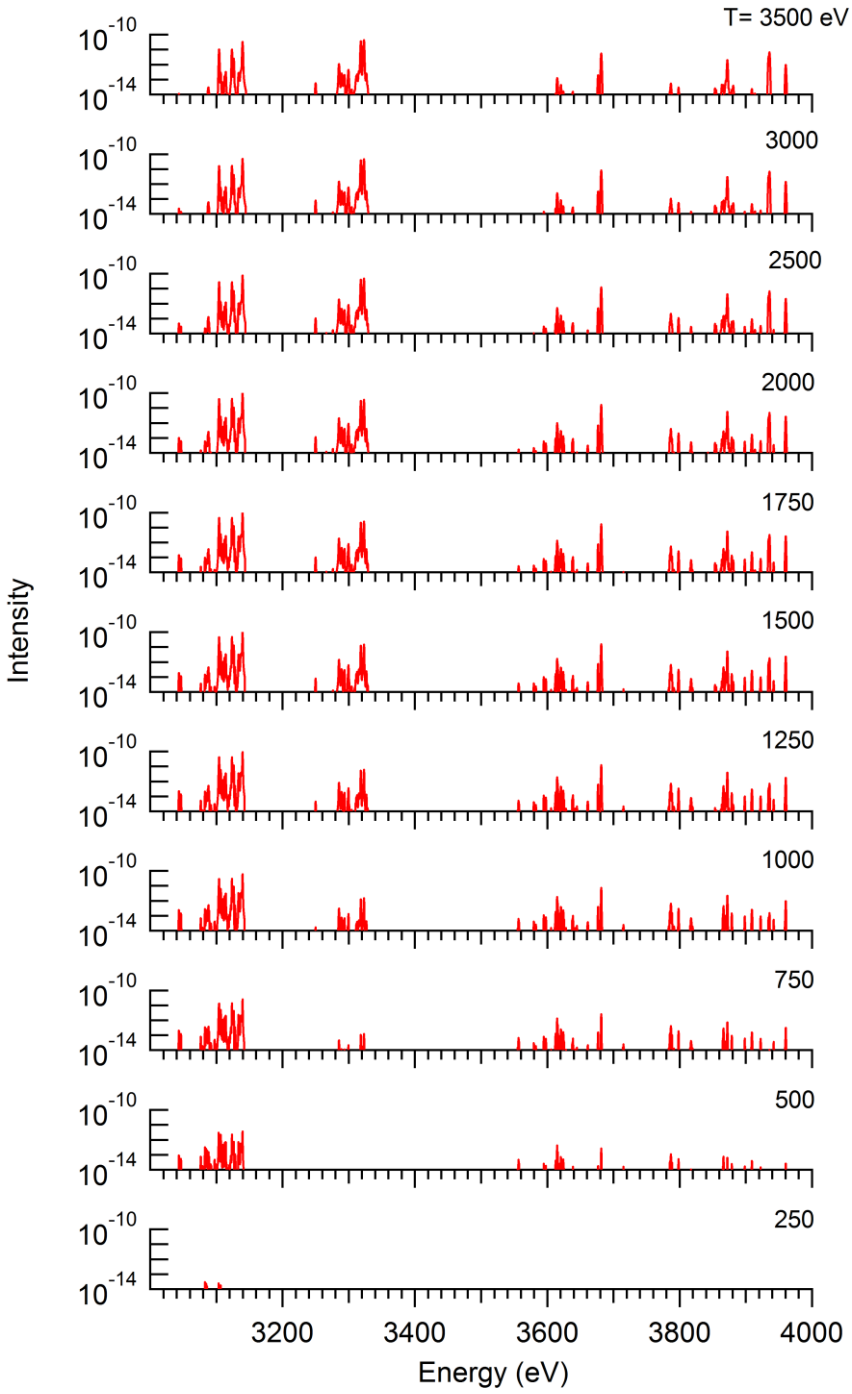

Figure 6. 7: FAC/NOMAD Calculated Ar Spectra for Maxwellian Distributed Electron Energies

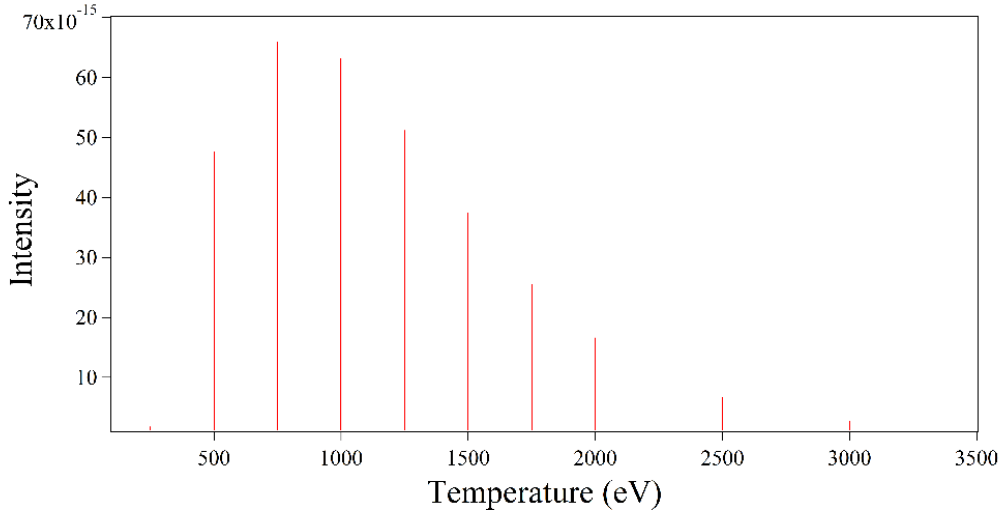

Figure 6. 8: Temperature Intensity Relationship for Be-like Ar Line at 3557 eV

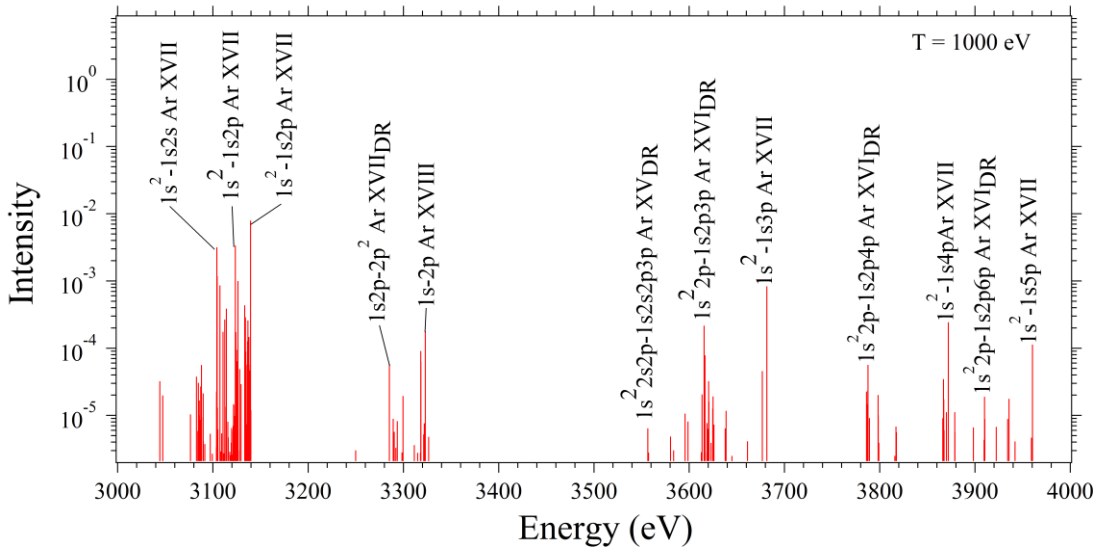

Figure 6. 9: Line identifications for Ar at a Temperature of 1000 eV

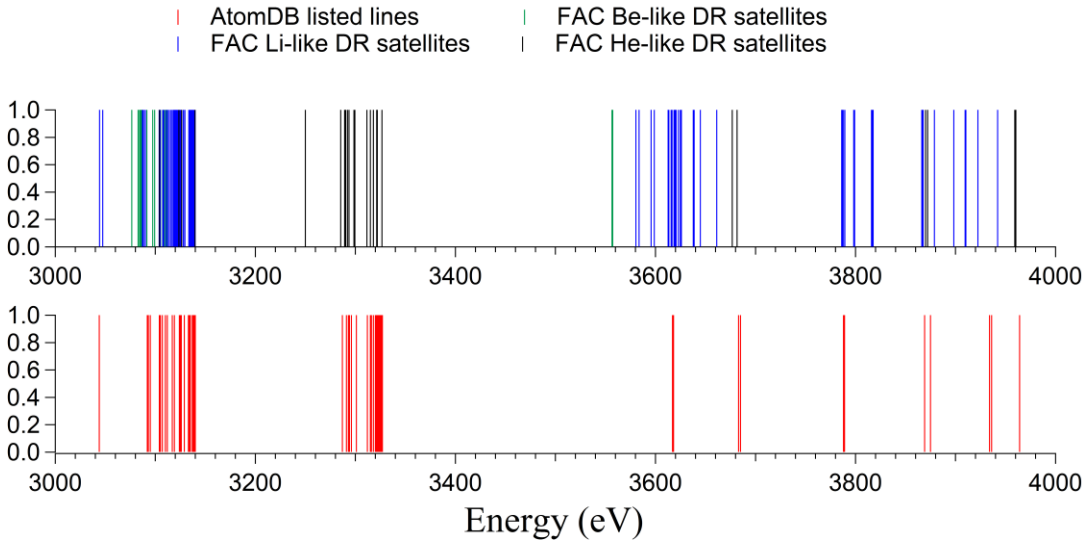

Figure 6. 10: Comparison of Calculated and AtomDB Listed Lines

(Top): FAC/NOMAD calculated Ar lines at 1000 eV. (Bottom) Lines listed in AtomDB at energies between 3000 and 4000 eV (listed at max temperatures).

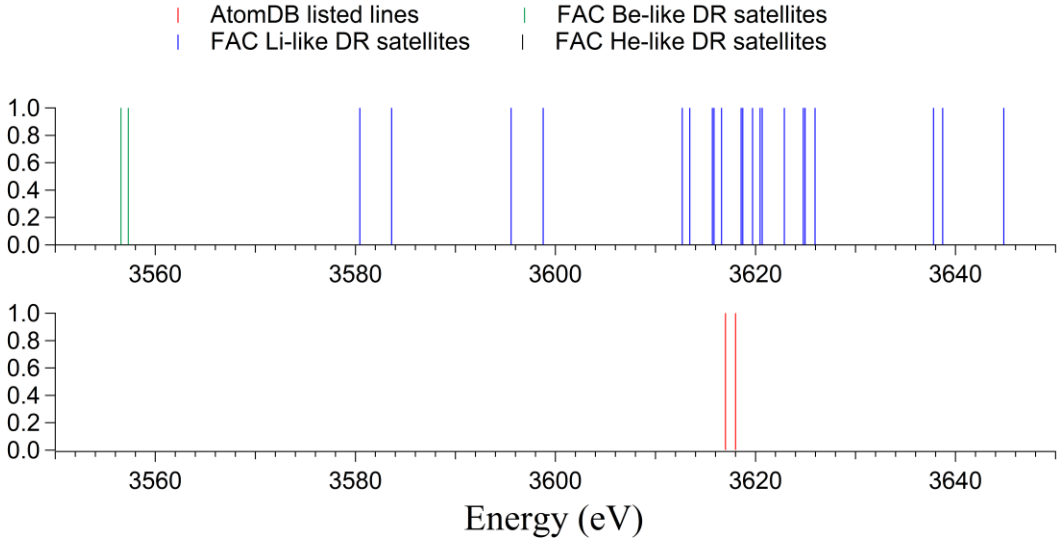

Figure 6. 11: Energy Range between 3550 and 3650 eV

CHAPTER SEVEN
CONCLUSIONS AND FUTURE WORK

The unidentified line measured in stacked spectra of galaxy clusters at around 3.55-3.57 keV was weak. Using the NIST EBIT we measured Be-like Ar lines at 3557 eV that were not included in the database used to fit the galaxy cluster spectra. If the low charge state lines we measured with the EBIT and calculated with FAC/NOMAD were not included in the spectral fits, it may be possible that they contribute some amount to the unidentified feature found by Bulbul et al. Additionaly the work by [14] show that low charge state ions may be more common than expected in galaxy clusters. This suggest that these lower charge state emission features may need to be added to the current model.

Continued work needs to be done to more accurately compare our measured results to those of AtomDB, including the conversion of our measured results from intensity to emissivity. The AtomDB database does not list weaker lines and insteads includes them in a pseudocontinium. Since these weak lines are not listed it is difficult to determine if they are being accurately accounted for. Based on the large number of unlisted lines, lack of inclusion, even in the pseudocontinium, could lead to over estimates of strong lines, and incorrect line energies and identifications.

APPENDICES

Appendix A

Supplemental Information

A.1 Raising and lowering operators:

$$l_+ = e^{i\phi}\left(\frac{\partial}{\partial\theta} + icot\theta\frac{\partial}{\partial\phi}\right)$$

$$l_- = e^{-i\phi}\left(-\frac{\partial}{\partial\theta} + icot\theta\frac{\partial}{\partial\phi}\right)$$

A.2 Matlab Code written to make cuts of surface plot.

```
%2-1 cut
clear all
clc
intensity = xlsread('Measured_Ge_detector.xlsx','Sheet5','C3:EF477');
[m,n] = size(intensity);
i = 1;
j=1;
two = zeros(n,1);
three = zeros(115,1);
for i =1:n

for j = 116:133
two(i)= two(i)+ intensity(j,i);
j = j+1;
end
i = i+1;
end

p=20;
i=1;
% 3-1 cut
for p =20:n

for j = 144:157
three(i)= three(i)+ intensity(j,p);
j = j+1;
end
i = i+1;
p = p+1;
end

% n=2 RR cut
RR = 0;
SV = round(xlsread('Measured_Ge_detector.xlsx','Sheet5','C1:EF1'));
sSV = length(SV);
```

```
k = 1;
diff = zeros(sSV,1);
for k =2:sSV
    diff(k) = SV(k)-SV(k-1);
end
l = 1;
s =1;
t = 113;
v = 127;
RR = zeros(n,1);
for l = 1:n
    t = t+ diff(l);
    v = v + diff(l);
    for s = t:v
    RR(l) = RR(l) + intensity(s,l);
    s = s+1;
    end
    l = l+1;
end

SV2 = xlsread('Measured_Ge_detector.xlsx','Sheet5','C2:EF2');
SV3 = xlsread('Measured_Ge_detector.xlsx','Sheet5','V2:EF2');
figure
plot(SV2,two,'b',SV3,three, 'g', SV2,RR, 'r');
xlabel('Shield Voltage (KV)')
ylabel('counts')
legend('n=2 cut','n=3 cut', 'RR cut')
figure
subplot(2,2,1);
plot(SV2,two,'b');
xlabel('Shield Voltage (KV)')
ylabel('counts')
title('n=2 cut')
subplot(2,2,2);
plot(SV3,three,'g');
xlabel('Shield Voltage (KV)')
ylabel('counts')
title('n=3 cut')

subplot(2,2,[3,4]);
plot(SV2,RR,'r');
xlabel('Shield Voltage (KV)')
ylabel('counts')
title('n=2 RR cut')
```

A.3: Detailed strong line identifications

Table A. 1: Line identification information for FAC used to label Figure 6. 9

charge state	Energy (eV)	Intensity	configuration		E level #		configuration		E level #	
He	3104.1468	3.1620E-03	0	1s2	1	J=0.0	1s1	2s1	2	J=1.0
He	3123.5325	3.3540E-03	0	1s2	1	J=0.0	1s1	2p1	4	J=1.0
He	3139.5802	7.8840E-03	0	1s2	1	J=0.0	1s1	2p1	7	J=1.0
He	3285.2631	5.8000E-05	1s1	2p1	7	J=1.0	0	2p2	-9	J=2.0
H	3322.9893	1.7770E-04	0	1s1	1	J=0.5	0	2p1	4	J=1.5
Be	3556.5645	6.4000E-06	2s1	2p1	4	J=2.0	2p1	3p1	-61	J=3.0
Li	3615.6881	2.1550E-04	0	2p1	3	J=1.5	2p1	3p1	-58	J=2.5
He	3681.5041	8.4610E-04	0	1s2	1	J=0.0	1s1	3p1	17	J=1.0
Li	3787.7093	5.6360E-05	0	2p1	3	J=1.5	2p1	4p1	-142	J=2.5
He	3872.0193	2.5320E-04	0	1s2	1	J=0.0	1s1	4p1	31	J=1.0
Li	3909.9372	1.8860E-05	0	2p1	3	J=1.5	2p1	6p1	-401	J=2.5
He	3960.2932	1.1270E-04	0	1s2	1	J=0.0	1s1	5p1	49	J=1.0

Appendix B

HPGe Detector Calibration

The HPGe detector provides an output spectra in counts versus channel number. From the measured HPGe detector data and the calculated data, convoluted to the HPGe detector response, a rough calibration was performed to convert the channel number to energy.

First the measured shield voltage was converted into electron beam energy taking the space charge, explained in Chapter 4, into account. Calculating the space charge is a straightforward procedure, but the ion cloud neutralization must also be considered. To find the neutralization factor, the n=3 to n=1 DR resonance peak was found from both the measured and calculated surface plot. The measured data showed that the 3-1 DR peak occurred at a shield voltage of 2795 kV. The calculated data showed that the peak occurred at a theoretical electron beam energy of 2740 eV. At this location, the space charge, corrected for ion cloud neutralization, must be 55 eV.

Next the space charge for a shield voltage of 2795 kV was calculated to be 202.80 V. Comparing this to the actual value of 55 eV indicates that the ion cloud neutralizes about 73% of the space charge at this energy. Assuming that the neutralization factor is a constant 73% of the calculated space charge, the remaining shield voltages were converted into corrected electron beam energy. A few calculated values are shown in Table A. 2.

Once the shield voltages were converted into corrected electron beam energies, they were compared to the calculated electron beam energies. The spectra were

calculated for electron beam energies between 2500 and 5000, in steps of 5 eV. The measured electron beam energies however were more random as seen in Table A. 2. The closest matching measured and calculated electron beam energies were selected. The spectra for the matching electron beam energies were opened in IGOR and spectral features were fit using the multipeak fitting package, as shown in Figure A. 1, where each spectra contains the residual, spectra with fit curve, and fit peaks. The peak energy of each peak were recorded in channel number for the measured spectra and energy for the calculated spectra.

Table A. 2: Space Charge Corrected Beam Energies

Beam Energy (KV)	V(r) (space charge at MDT)	Corrected Beam Energy (eV)
2.312	223.0	2251.5
2.331	222.1	2270.8
2.343	221.5	2282.9
2.433	217.4	2374.1
2.485	215.1	2426.7
2.535	213.0	2477.2
2.585	210.9	2527.8
2.585	210.9	2527.8
2.62	209.5	2563.2
2.634	208.9	2577.3
2.684	207.0	2627.9
2.73	205.2	2674.3
2.735	205.0	2679.4
2.75	204.5	2694.6
2.765	203.9	2709.7
2.782	203.3	2726.9
2.795	202.8	2740.0
2.812	202.2	2757.2
2.826	201.7	2771.3
2.84	201.2	2785.4

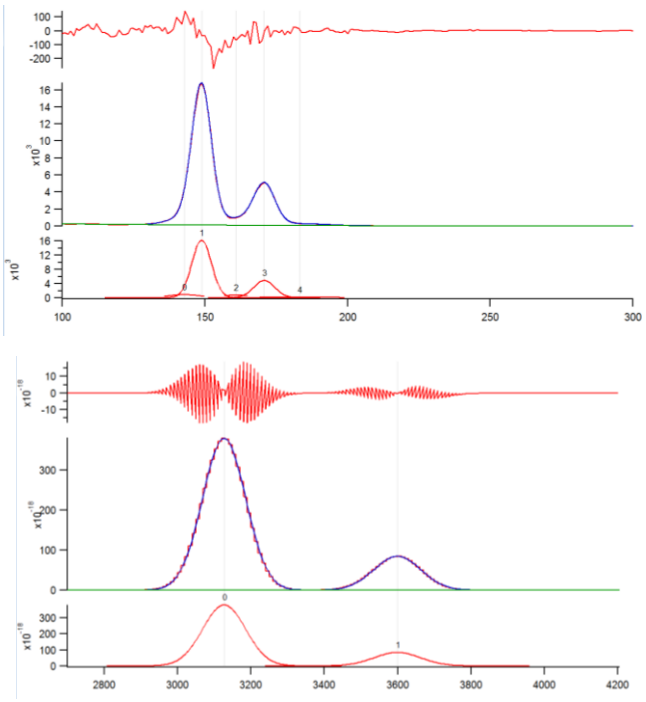

Figure A. 1: Fitted Measured and Calculated Spectra

Top: Measured spectra a 2740 eV electron beam energy. Bottom: Calculated spectra at 2740 eV.

Finally the n=1 and n=3 radiative recombination (RR) peaks were also used for calibration. The measured spectra at 4457 eV was used to fit the RR peaks and get the peak location in channel number. For the n=1 RR peak, the energy of the photon should be the electron beam energy plus the ionization energy, where the He-like Ar ionization energy is 4120.6655 eV. This gives the theoretical photon energy a value of 8577 eV for the n=1 RR peak at 4457 eV beam energy.

It is known that the n=3 RR peak is at the same energy as the n=3-1 DR peak at the resonance. This means the n=3 RR photon energy is 3126.94 eV (the measured n=3-1 DR energy) at a beam energy of 2740 eV. Since the RR photon energy scales with the electron beam energy, at 4457 eV beam energy, the photon energy of the n=3 RR peak should theoretically be 4843.94 eV. (4457-2740+3126.94)

Using the channel/energy matching of the calculated spectra and the RR peaks, shown in Table A. 3, a plot was created to convert channel number to energy, as shown in Figure A. 2.

Table A. 3: Measured and Calculated Electron Beam Energies and Fits

Beam Energy	Measured peak location (channel)	Measured sigma	Theoretical peak location (eV)	Theoretical sigma
2220	147.85	0.009184	3106.33	0.074726
2230	147.845	0.009112	3104.14	0.074646
2710	148.807	0.107507	3126.55	0.081005
2710	171.9	0.107638	3606.8	0.223544
2740	148.86	0.030032	3126.94	0.077309
2740	170.798	0.107759	3598.8	0.364224
2785	148.218	0.043845	3124.33	0.075402
2785	170.545	0.089273	3594.55	1.03205
3165	148.893	0.015116	3124.96	0.074645
3270	148.87	0.010087	3124.29	0.074552
4457	230.296	0.292752	4843.94	0.077309
4457	408.374	0.201214	8577	0.0005
2695	148.303	0.05241	3123.58	0.082917
2695	171.752	0.054111	3609.43	0.184357
3030	148.865	0.015968	3135.29	0.07451
3150	148.71	0.015714	3123.69	0.074719

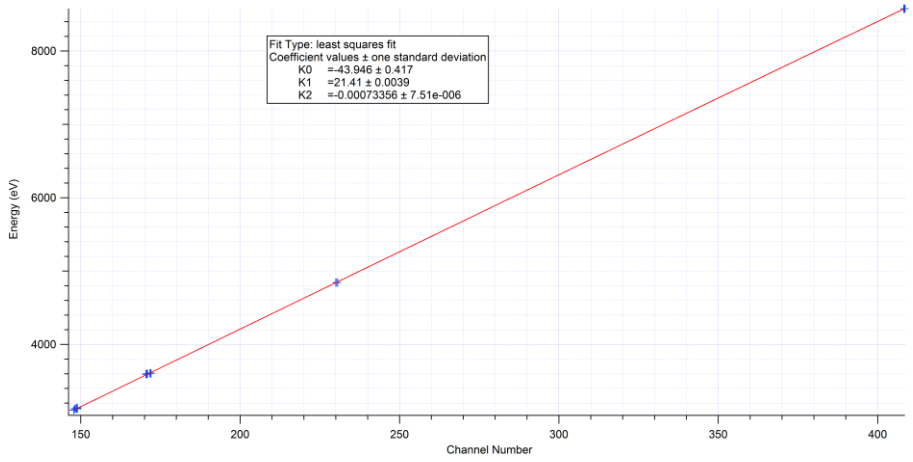

Figure A. 2: Calibration Plot

REFERENCES

[1] E. Bulbul, M. Markevitch, A. Foster, R. K. Smith, M. Loewenstein, and S. W. Randall, Astrophys. J. **789**, 13 (2014).

[2] Y. V Ralchenko and Y. Maron, J. Quant. Spectrosc. Radiat. Transf. **71**, 609 (2001).

[3] M. F. Gu, Can. J. Phys. **86**, 675 (2008).

[4] D. W. Savin, N. S. Brickhouse, J. J. Cowan, R. P. Drake, S. R. Federman, G. J. Ferland, A. Frank, M. S. Gudipati, W. C. Haxton, E. Herbst, S. Profumo, F. Salama, L. M. Ziurys, and E. G. Zweibel, Rep. Prog. Phys. **75**, 36901 (2012).

[5] A. Boyarsky, O. Ruchayskiy, D. Iakubovskyi, and J. Franse, Phys. Rev. Lett. **113**, 1 (2014).

[6] O. Urban, N. Werner, S. W. Allen, A. Simionescu, J. S. Kaastra, and L. E. Strigari, MNRAS **451**, 2447 (2015).

[7] D. Iakubovskyi, E. Bulbul, A. R. Foster, D. Savchenko, and V. Sadova, (2015).

[8] H. Collaboration, F. A. Aharonian, H. Akamatsu, F. Akimoto, S. W. Allen, L. Angelini, K. A. Arnaud, M. Audard, H. Awaki, M. Chernyakova, M. P. Chiao, P. Coppi, E. Costantini, J. De Plaa, J.-W. Den Herder, and C. Done, (2016).

[9] D. Malyshev, A. Neronov, and D. Eckert, Phys. Rev. D **90**, 103506 (2014).

[10] M. E. Anderson, E. Churazov, and J. N. Bregman, MNRAS **452**, 3905 (2015).

[11] T. Tamura, R. Iizuka, Y. Maeda, K. Mitsuda, and N. Y. Yamasaki, Publ. Astron. Soc. Japan **67**, 23 (2015).

[12] E. Carlson, T. Jeltema, and S. Profumo, J. Cosmol. Astropart. Phys. **2015**, 9

(2015).

[13] N. Sekiya, N. Y. Yamasaki, and K. Mitsuda, Publ. Astron. Soc. Japan **68**, S31 (2016).

[14] L. Gu, J. Kaastra, A. J. J. Raassen, P. D. Mullen, R. S. Cumbee, D. Lyons, and P. C. Stancil, A&A **584**, (2015).

[15] C. Shah, S. Dobrodey, S. Bernitt, R. Steinbrügge, J. R. C. López-Urrutia, L. Gu, and J. Kaastra, 7 (2016).

[16] C. J. Foot, *Atomic Physics* (Oxford University Press, 2005).

[17] A. K. Pradhan and S. N. Nahar, *Atomic Astrophysics and Spectroscopy* (Cambridge University Press, 2011).

[18] http://quantummechanics.ucsd.edu/ph130a/130_notes/node210.html, (n.d.).

[19] Http://quantummechanics.ucsd.edu/ph130a/130_notes/node233.html, (n.d.).

[20]Https://upload.wikimedia.org/wikipedia/commons/thumb/e/ec/Scheme_of_Madelung_Rule.jpg/220px-Scheme_of_Madelung_Rule.jpg, (n.d.).

[21] https://web.njit.edu/~gary/728/assets/planck.jpg, (n.d.).

[22] R. K. Smith, N. S. Brickhouse, D. A. Liedahl, and J. C. Raymond, Astrophys. J. **556**, L91 (2001).

[23] G. X. Chen, R. K. Smith, K. Kirby, N. S. Brickhouse, and B. J. Wargelin, Phys. Rev. A **74**, 42709 (2006).

[24] R. K. Smith, G.-X. Chen, K. Kirby, and N. S. Brickhouse, Astrophys. J. **700**, 679 (2009).

[25] C. Biedermann, R. Radtke, and K. B. Fournier, Phys. Rev. E **66**, 66404 (2002).

[26] A. J. Smith, P. Beiersdorfer, V. Decaux, K. Widmann, K. J. Reed, and M. H. Chen, Phys. Rev. A **54**, 462 (1996).

[27] A. J. Smith, P. Beiersdorfer, K. Widmann, M. H. Chen, and J. H. Scofield, Phys. Rev. A **62**, 52717 (2000).

[28] R. Ali, C. P. Bhalla, C. L. Cocke, and M. Stockli, Phys. Rev. Lett. **64**, 633 (1990).

[29] D. R. DeWitt, D. Schneider, M. W. Clark, M. H. Chen, and D. Church, Phys. Rev. A **44**, 7185 (1991).

[30] J. D. Gillaspy, Phys. Scr. **T71**, 99 (1997).

[31] Gillaspy, John D, Ratliff, Laura P, Roberts, James R, Takacs, and Endre, *Highly Charged Ions, Publications of the EBIT Project, 1993-2001* (2001).

[32] John Gillaspy, editor , *Trapping Highly Charged Ions: Fundamentals and Applications* (Nova Science Publishers, Inc., 2001).

[33] J. V. Porto, I. Kink, and J. D. Gillaspy, Rev. Sci. Instrum. **71**, 3050 (2000).

[34] E. P. Bertin, *Principles and Practice of X-Ray Spectrometric Analysis* (Springer US, Boston, MA, 1975).

[35] Y. Zou and R. (Roger) Hutton, *Handbook for Highly Charged Ion Spectroscopic Research* (Taylor & Francis, 2012).

[36] S. Brennan, P. L. Cowan, R. D. Deslattes, A. Henins, D. W. Lindle, and B. A. Karlin, Rev. Sci. Instrum. **60**, 2243 (1989).

[37] http://www.crystals.saint-gobain.com/sites/imdf.crystals.com/files/johann_geo.png, (n.d.).

[38] R. Barnsley, N. J. Peacock, J. Dunn, I. M. Melnick, I. H. Coffey, J. A. Rainnie, M.

R. Tarbutt, and N. Nelms, Cit. Rev. Sci. Instrum **74**, (2003).

[39] S. B. Howell, (2000).

[40] B. (Burkhard) Beckhoff, B. Kanngieber, N. Langhoff, R. Wedell, and H. Wolff, editors , *Handbook of Practical X-Ray Fluorescence Analysis* (Springer, 2006).

[41] Y. A. Podpaly, J. D. Gillaspy, J. Reader, and Y. Ralchenko, J. Phys. B At. Mol. Opt. Phys. **47**, 95702 (2014).

[42] D. Kilbane, G. O'Sullivan, Y. A. Podpaly, J. D. Gillaspy, J. Reader, and Y. Ralchenko, Eur. Phys. J. D **68**, 222 (2014).

[43] J. Reader, J. D. Gillaspy, D. Osin, and Y. Ralchenko, J. Phys. B At. Mol. Opt. Phys. **47**, 145003 (2014).

[44] B. L. Henke, E. M. Gullikson, and J. C. Davis, At. Data Nucl. Data Tables **54**, 181 (1993).

[45] C. Shah, S. Dobrodey, S. Bernitt, R. Steinbrügge, J. R. Crespo López-Urrutia, L. Gu, and J. Kaastra, (2016).